# Oxidation state of arc mantle revealed by partitioning of V, Sc and Ti between mantle minerals and basaltic melts

**Article** · April 2019

DOI: 10.1029/2018JB016731

CITATIONS
7

READS
435

**6 authors**, including:

Jintuan Wang
Chinese Academy of Sciences
**4** PUBLICATIONS **47** CITATIONS
SEE PROFILE

Eiichi Takahashi
Chinese Academy of Sciences
**172** PUBLICATIONS **7,610** CITATIONS
SEE PROFILE

Le Zhang
Chinese Academy of Sciences
**55** PUBLICATIONS **245** CITATIONS
SEE PROFILE

Xingcheng Liu
Chinese Academy of Sciences
**11** PUBLICATIONS **140** CITATIONS
SEE PROFILE

Wang Jintuan (Orcid ID: 0000-0002-6682-9036)
Xiong Xiaolin (Orcid ID: 0000-0003-2054-3339)
Liu Xingcheng (Orcid ID: 0000-0002-1910-1376)

# Oxidation state of arc mantle revealed by partitioning of V, Sc and Ti between mantle minerals and basaltic melts

**Jintuan Wang[1,2], Xiaolin Xiong[1], Eiichi Takahashi[1], Le Zhang[1], Li Li[1], Xingcheng Liu [1]**

[1] State Key Laboratory of Isotope Geochemistry, CAS, Guangzhou 510640, China.

[2] College of Earth and Planetary Sciences, University of the Chinese Academy of Sciences, Beijing 100049, China.

Corresponding author: Xiaolin Xiong (xiongxl@gig.ac.cn)

**Key Points:**

- In addition to oxygen fugacity, temperature exerts a significant control on V partitioning during mantle melting.
- Considering the temperature effect on V partitioning, similar V/Ti or V/Sc ratios between arc basalts and MORBs indicate a more oxidized arc mantle.
- Modelling results from V-Ti systematics indicate that arc mantle is ~0.9 log units higher in $fO_2$ than oceanic mantle.



This article has been accepted for publication and undergone full peer review but has not been through the copyediting, typesetting, pagination and proofreading process which may lead to differences between this version and the Version of Record. Please cite this article as doi: 10.1029/2018JB016731

**Abstract**

Whether arc mantle is more oxidized than oceanic mantle is persistently debated. The behavior of multivalent vanadium (V) is oxygen fugacity ($fO_2$) sensitive, and the ratios of V to a homovalent element (e.g. Sc, Ti or Yb) in basalts were commonly used as $fO_2$ proxies. Similar ratios, such as V/Sc, between arc basalts and mid-ocean ridge basalts (MORBs) were previously taken as evidence for similar $fO_2$s in their mantle sources. However, this claim may be problematic because elemental ratios are primarily controlled by partition coefficients (D-values), which are further affected by various parameters. Here, we determined D-values of V and other transition elements between mantle minerals and basaltic melts at typical arc T-P-$H_2O$ conditions and variable $fO_2$s. Combining experimental results with published data, the effects of $fO_2$, T , P and phase compositions on $D_V$, $D_{Sc}$ and $D_{Ti}$ for olivine, orthopyroxene (opx), clinopyroxene (cpx) and spinel were evaluated using multiple linear regressions. The results show that $D_V$ values for these four minerals all increase with decreasing $fO_2$ and temperature, leading to higher $D_V/D_{Sc}$ and $D_V/D_{Ti}$ ratios at low temperatures than those at high temperatures given a certain $fO_2$. Thus, similar V/Sc and V/Ti ratios between arc basalts and MORBs reflect a relatively oxidized arc mantle due to its lower melting temperatures. In light of the highly incompatible behavior of Ti during mantle melting, V-Ti systematics are regarded to be more reliable than V-Sc systematics in the $fO_2$ estimation. Partial melting modelling results using V-Ti systematics reveal that arc mantle is, on average, ~0.9 log units higher in $fO_2$ than oceanic mantle.

**Plain Language Summary**

The oxidation state of the Earth`s mantle, often expressed as oxygen fugacity ($fO_2$), could control the behavior of multivalent elements, and thus exert a significant influence on the formation of magmatic ore deposits and the secular evolution of Earth`s atmosphere. Whether arc mantle is more oxidized than oceanic mantle remains a controversial topic. As a multivalent element, partitioning behavior of vanadium is $fO_2$ sensitive and is capable of tracking mantle redox state. However, except $fO_2$, other factors (temperature, pressure, and phase composition) that may affect vanadium partitioning behavior have not been clearly evaluated. Here we conducted high temperature and pressure experiments to determine partition coefficients of vanadium during mantle melting under various $fO_2$ conditions. Combining our and published data, we evaluated the effects of $fO_2$, T, P and compositions of mineral and melt on the vanadium partitioning using multiple linear regressions. The results indicate that, in addition to $fO_2$, temperature exerts a significant control on the vanadium partitioning. Additionally, we estimated $fO_2$ of the arc mantle via numerical modelling using appropriate partition coefficients for vanadium. Our results clarify and reconcile the discrepancies between previous studies and reveal that arc mantle is generally ~10 times more oxidized than oceanic mantle.

## 1 Introduction

Oxygen fugacity ($fO_2$) plays key roles in the evolution of Earth's lithosphere and atmosphere (Kump et al., 2001; Wood et al., 1990) by controlling the speciation and behavior of multivalent elements during mantle melting and volcanic eruption. The relative $fO_2$ of the mantle decreases with depth (Frost and McCammon, 2008; Rohrbach and Schmidt, 2011); however, whether there is a lateral variation of $fO_2$ in the top of the upper mantle remains a controversial issue. Arcs and mid-ocean ridges are two of the most important tectonic settings where mantle-derived magmas erupt. Arc magmas are demonstrably more oxidized than mid-ocean ridge basalts (MORB) (Christie et al., 1986; Carmichael, 1991). However, whether the mantle source of arc magmas is also more oxidized than that of MORBs is strongly debated due to the conflicting results from different approaches of $fO_2$ estimation. Oxybarometers based on Fe valence states, such as the $Fe^{3+} \leftrightarrow Fe^{2+}$ mineral equilibrium $6Fe_2SiO_4$ (olivine) + $O_2 = 3Fe_2Si_2O_6$ (opx) + $2Fe_3O_4$ (spinel) in mantle xenoliths (Ballhaus, 1993; Ballhaus et al., 1990; Parkinson and Arculus, 1999) and basalts (Evans et al., 2012), as well as the $Fe^{3+}/Fe_T$ ratios in basaltic glasses (Bézos and Humler, 2005; Cottrell and Kelley, 2011) and olivine-hosted melt inclusions (Brounce et al., 2014, 2015; Kelley and Cottrell, 2009, 2012), indicated that arc mantle is more oxidized relative to the MORB source. In contrast, V/Sc and $Zn/Fe_T$ studies (Lee et al., 2005, 2010) argued that arc mantle and oceanic mantle are similar in $fO_2$ based on the seemingly similar V/Sc and $Zn/Fe_T$ ratios between primitive arc basalts and MORBs.

Previous V/Sc and $Zn/Fe_T$ studies ( Lee et al., 2005, 2010) have pointed out that (1) the partitioning behaviors of V and Fe during mantle melting are redox-sensitive because of their variable valence states (V: 2+, 3+, 4+ and 5+; Fe: 2+ and 3+), whereas, Sc and Zn are homovalent (Sc: 3+ and Zn: 2+) and redox-insensitive over the upper mantle $fO_2$ range; (2) V and Sc are incompatible and Zn and Fe have similar compatibilities during the early crystallization of olivine. Thus, V/Sc and $Zn/Fe_T$ ratios should preserve a record of $fO_2$ in the mantle source. However, elemental ratios of primitive basalts are mainly controlled by mineral/melt D-values during mantle melting, which are dependent not only on $fO_2$, but also on temperature (T), pressure (P) and phase compositions. Therefore, V/Sc and $Zn/Fe_T$ ratios may not be an accurate $fO_2$ proxy unless, in addition to $fO_2$, the effects of T, P and phase compositions on the D-values are also addressed. Despite this, published $D_V$ and $D_{Sc}$ values are mainly obtained from anhydrous experiments performed at one atmosphere or at high pressure and reduced conditions (Canil, 1997, 1999; Canil and Fedortchouk, 2000; Davis et al., 2013; Laubier et al., 2014; Mallmann and O'Neill, 2009; Papike et al., 2013; Pertermann et al., 2004; Righter et al., 2006; Toplis and Corgne, 2002), and published $D_{Zn}$ values are scarce (Davis et al., 2013; Le Roux et al., 2011). One study (Jackson et al., 2010) addressed mineral/melt partitioning of V and Sc during partial melting of the mantle wedge, but did not report specific D-values. Therefore, strictly speaking, there are no systematic V, Sc and Zn partitioning data pertinent to arc mantle melting. The V/Sc study (Lee et al., 2005) performed mantle melting modelling beneath arcs and ridges using mineral/melt $D_V$-values from one atmosphere experiments. These $D_V$ values might be inappropriate because mantle melting occurs at high pressures, and melting temperatures at arcs and ridges are quite different. To examine the $fO_2$ difference between mantle wedge and oceanic mantle, accurate mineral/melt D-values pertinent to the generation conditions of primitive arc basalts and MORBs are required.

In this study, we conducted piston-cylinder experiments to determine the D-values of V and other transition elements between mantle minerals and basaltic melts. The experiments were performed at typical arc P-T-$H_2O$ conditions and variable $fO_2$s. Combining our results with published data, we evaluated the effects of $fO_2$, T, P and phase compositions on $D_V$, $D_{Sc}$

and $D_{Ti}$ and quantitatively addressed the effect of each variable by multiple linear regressions. In addition, we estimated mantle source $fO_2$s of the primitive arc basalts and MORBs considering the P-T conditions of magma generation, and using the appropriate D values.

## 2 High Pressure and High Temperature Experiments

### 2.1 Starting materials and sample capsules

To produce mantle minerals in equilibrium with basaltic melts at experimental conditions, three starting materials (SM1, SM2 and SM3; Table 1) were prepared from a synthetic high MgO basalt and a synthetic KLB-1 peridotite. The synthesized high-Mg basalt (SM1) was doped with FRTEs (first row transition elements), REEs (rare earth elements), LILEs (large ion lithosphere elements) and Cs at levels of < 200 ppm, except for Cr and Zn at ~1000 ppm (Table 1). This composition was prepared by mixing reagent grade oxides $SiO_2$, $Al_2O_3$, $Fe_2O_3$, MgO, $TiO_2$, MnO, NiO, $P_2O_5$ and $Cr_2O_3$, and carbonates $CaCO_3$, $Na_2CO_3$ and $K_2CO_3$. Trace elements were doped to this mixture as oxides, except for Cs (added as CsCl). The mixture was homogenized with an agate mortar and pestle by grinding under acetone for 2 h. The ground mixture was then decarbonated in a Pt crucible at 1000 $^oC$ for 10 h and fused in the same Pt crucible at 1500 $^oC$ for 2 h. To guarantee homogeneity, another round of grinding and fusion was performed. Several aliquots of the quenched glass were left for both electron probe micro-analyzer (EPMA) and laser ablation inductively coupled plasma mass spectrometry (LA-ICP-MS) analyses. To synthesize the KLB-1 peridotite, we first synthesized a glass composition equal to MgO-subtracted KLB-1 peridotite following the aforementioned procedures. To make the final KLB-1 composition, magnesium was added into the Mg-free glass as MgO and homogenized by grinding for 2 h under alcohol. In total, three starting materials were prepared: SM1 is the synthesized high MgO basalts, and SM2 and SM3 are mixtures of the high MgO basaltic glass and KLB-1 peridotite composition at ratios of 4.7:1 and 2.5:1, respectively. The prepared starting material powders were stored in an oven at 120 $^oC$ until use.

Gold-palladium alloy capsules with iron content of 0, 0.5, 1.0 or 1.5 wt% were used as the sample containers (ID: 2.7mm; OD: 3mm; Length: ~6mm) (Table 2). The different alloy compositions produce variable $fO_2$ values during experiments that are expected to cover $fO_2$ range of the arc mantle (see section 2.3). Iron-free alloy capsules were used to produce relatively oxidized ambient conditions, and iron-bearing alloy capsules were used not only to produce relatively reduced ambient conditions, but also to minimize effectively the Fe-loss at reduced conditions. Some of the sample capsules contain 2 wt% Cu, which is used to buffer Cu content of the experimental charges in order to obtain accurate Cu partition coefficients (Liu et al., 2014, 2015). According to the typical $H_2O$ contents of near-primitive arc basalts (2–6 wt% $H_2O$, Plank et al., 2013; Wallace, 2005), less than 6.0 wt% $H_2O$ was added into the starting materials. For each sample, ~10 mg of the starting material powder together with water was packed into the capsule. $H_2O$ was injected into the capsule with a micro-syringe before the powder was loaded. The capsule was pinched and welded shut with a LAMPERT PUK U3 welding machine and was checked by drying and weighing to ensure no $H_2O$ leakage during sample preparation.

### 2.2 Experimental procedures

All the experiments were conducted at 0.5–3.0 GPa, and 1150–1350 $^oC$ (Table 2) on a Rockland piston-cylinder apparatus. The assembly in the pressure vessel is composed of

graphite furnace ± Pyrex glass + $BaCO_3$ sleeve + MgO inserts. For each experiment, the sample capsule was positioned at the center of the furnace. The thermocouple wires were housed in a two-bore alumina sleeve, with the junction in contact with an alumina disk (0.5 mm thickness) at the top of the sample capsule. Experiments at 2.0–3.0 GPa were performed using the 1/2 inch assembly and those at 0.5–1.5 GPa were conducted using the 3/4 inch assembly. During the experiments, pressures were automatically regulated to the set-point. Experimental temperatures were controlled using a Eurotherm controller and measured with an S-type (Pt-$Pt_{90}Rh_{10}$) thermocouple with variations less than ± 2 °C. No pressure effect on electromotive force (EMF) of the thermocouple was corrected. Fraction corrections of +13 % and 0 % were respectively applied for the 1/2 and 3/4 inch assemblies (See Liu et al., (2014) for the correction methods). The actual pressures are believed to be accurate to 0.1 GPa and the temperature gradients along the samples are expected to be less than 15 °C. Experimental durations varied from 20 to 50 h. Each of the experiments was terminated by turning off electric power to the heater, then unloading slowly. The recovered capsules were sectioned, mounted in epoxy resin and polished for optical observations and subsequent micro-beam analyses.

### 2.3 Producing a range of $fO_2$

Controlling $fO_2$ in piston-cylinder experiments is a difficult task. A particular problem is the removal or addition of hydrogen and iron from or into the sample charge, due to $H_2$ permeability and Fe alloying with the metal capsule. Carbon permeability in some cases can further complicate this problem. For an experiment using a single noble metal capsule (without redox buffer), $fO_2$ of the experimental charge is governed by complex interactions between furnace assembly, capsule metal and the starting material. The final $fO_2$ is achieved via H diffusion through the capsule wall, Fe alloying with the capsule metal and water dissociation within the capsule. Initial oxidation state of the starting material can also affect the final $fO_2$, but this effect is usually limited because of the small amount of the starting material. The starting material will lose or gain Fe during an experiment, depending on the capsule material and experimental T-P-X-$fO_2$ conditions. For experiments using a single capsule, the hydrogen fugacity ($fH_2$) is largely controlled by the assembly, and the availability of $H_2$ from the assembly to the samples depends on how well the assembly is dried (Luth, 1989). In addition, experimental pressure and temperature could also influence the $fH_2$ in the pressure vessel. In summary, any factor that influences Fe loss/gain and $fH_2$ in the pressure vessel will affect the final experimental $fO_2$; thus, a range of $fO_2$ is expected in a series of experiments with different P-T conditions and sample capsules.

Using single AuPd capsules and standard furnace assemblies such as NaCl-Pyrex, Talc-Pyrex and $BaCO_3$-Pyrex, a range of $fO_2$ values have been reported (FMQ+1 to FMQ+3.6, FMQ = fayalite-magnetite-quartz buffer) (e.g., Pichavant et al., 2002; Matjuschkin et al., 2015). Combinations of these assemblies and AuPd capsule are able to produce relatively oxidized conditions. To achieve $fO_2$s lower than FMQ+1 and to minimize Fe loss at reduced conditions, Fe-presaturated AuPd capsules were used (Kägi et al., 2005; Barr and Grove, 2010). Kägi et al. (2005) preconditioned the $Au_{90}Pd_{10}$ capsules at 1.0 GPa and 1200 °C, and achieved $fO_2$ values of around FMQ-1 with the resulting AuPd alloys containing 0.5 to 0.7 wt% Fe. In this study, we used the $BaCO_3$+Pyrex assembly and AuPd alloy capsules with different iron contents (0, 0.5, 1.0, 1.5 wt%), and thus a range of $fO_2$ values were expected in our experiments (see the calculated results in section 4.3 and Table 2).

## 3 Analytical Methods

### 3.1 Electron Microprobe

Major element oxides (wt%) of minerals and quenched melts in the run products (Figure 1) were analyzed with the JEOL JXA-8230 EPMA. The analyses were performed in wavelength-dispersive mode. Silicate minerals and oxides were used as standards with the ZAF matrix correction applied. The analytical conditions were 15 kV accelerating voltage, 20 nA beam current and 1 μm diameter beam size for minerals, and 10 nA beam current and 20 μm diameter beam size for quenched melts. The peak counting time was 10 s for Na and K and 20 s for the other elements. A dry glass XT168, which was repeatedly analyzed by Xiong et al. (2005), was used as a secondary standard to monitor the analytical precision and accuracy. Analytical accuracy is better than ± 2% relative for $SiO_2$, $Al_2O_3$ and CaO, ± 5% relative for $TiO_2$, FeO, MnO, MgO, $K_2O$ and $P_2O_5$, and ± 10% relative for $Na_2O$. Mass balance calculations were performed to obtain phase proportions, iron-loss/gain and $H_2O$-loss/gain in the run products. The results revealed < 20 wt% relative Fe-loss/gain and < 5% absolute $H_2O$-loss/gain for most of the runs (Table 2).

Vanadium, Co and Zn contents in spinel, as well as Au, Pd, Fe, Cu and Zn contents in the capsules were also analyzed with EPMA. Standards for V, Co and Zn analyses in spinel are metal V, skutterudite and willemite, respectively. In the analyses of Au, Pd, Fe, Cu and Zn in sample capsules, pure metals were used as standards. Analytical conditions for both spinel and capsule metals were 15 kV accelerating voltage, 50 nA beam current and 1 μm diameter beam size. The peak counting time was 60 s for V, Co and Zn in spinel, and 20 s for Au, Pd, Fe, Cu and 60 s for Zn in the capsules. We analyzed rims of the alloy capsules adjacent to the silicate melts (within 10 μm of the melts). To further check the Fe homogeneity across the alloy capsules walls, we also analyzed profiles of Fe content across the sample capsules in two representative runs.

### 3.2 LA-ICP-MS

Trace element concentrations (ppm) in minerals and quenched melts were measured by LA-ICP-MS at Guangzhou Institute of Geochemistry, for which a Resolution S155 Resonetic 193nm ArF excimer laser was attached to an Agilent 7900a ICP-MS. Helium was used as carrier gas and $N_2$ was added to optimize the detection limits. The energy density was 4 J/cm$^2$ and the repetition rate was set at 6 Hz. The laser spots were positioned at the crystal-free melt pools and the rims of minerals. We found overgrowth or slightly compositional zoning in some cpx grains in several runs such as shown in Figure 1. In these cases, we chose to analyze crystals without zonation and overgrowth. Beam sizes were 13 or 19 μm for minerals and 19–44 μm for quenched melts. NIST SRM 610 glass was used as the external standard and SRM 612 glass was used as the monitor standard. EPMA analyses of Ca (melt, plagioclase, cpx), Mg (olivine, opx) and Al (garnet) were used as the internal standards. For each run product, typically three to six analyses were performed on each phase. During the analysis of minerals, the time-resolved signal of Cs was used to monitor melt contamination. Cs is highly incompatible in mantle minerals and thus contamination from melt can be easily recognized by the elevated Cs signals. Analyses were discarded if Cs contamination was detected. In addition, olivine, opx and cpx could contain minute spinel inclusions. During data processing, spinel contamination can be identified by sharp increases in Cr, Al and V signals. Analyses were also discarded if spinel signals were detected. Judging from the SRM 612 monitor standard, reproducibility (1σ) for Sc, Ti, V, Cr, Mn, Co, Ni and Cu is typically < 5% relative and for Zn is ~11 % relative.

3.3 Comparison of V analyses between EPMA and LA-ICP-MS.

Because $D_V$ values for spinel were obtained from EPMA analyses in spinels and LA-ICP-MS analyses in melts, accuracy of the V analyses by EPMA requires to be demonstrated. Here, we compared V analyses between the EPMA and LA-ICP-MS techniques in some experimental run products (opx, cpx and quenched melt). The results exhibit good consistency between these two techniques for V content higher than ~250 ppm (Figure 2, data in Table S2 h), verifying the reliability of our EPMA V analyses in spinels because they all have V contents > 300 ppm. The results also exclude the potential Ti interference problem in our V analyses of spinels. During EPMA analysis, the Kα peak of V may be overlapped by the Kβ peak of Ti, when Ti content is sufficiently high in the sample (Fialin et al., 1997). $TiO_2$ contents in spinels from this study was lower than 1.0 wt%, which is within the ranges of $TiO_2$ contents in opxs (< 0.35 wt%), cpxs (< 1.0 wt%) and quenched melts (< 1.76 wt%). The good agreement between the V analyses of EPMA and LA-ICP-MS demonstrates that Ti interference on V is negligible in the EPMA analyses when $TiO_2$ content < 1.76 wt%.

## 4. Results

4.1 General observations and phase compositions

Thirty-eight runs successfully produced basaltic melts saturated with 2 to 5 mantle phases, including olivine, opx, cpx, spinel, garnet and plagioclase (Figure 1 and Table 2). For all the run products, crystals of these minerals ranged from less than 20 μm to larger than 100 μm and at least one mineral in each run was large enough for both EPMA and LA-ICPMS analyses. Spinels were usually less than 10 μm and could only be analyzed by EPMA. Some cpxs showed overgrowth or slight compositional zonation and some grains of olivine, opx and cpx contained minute spinel inclusions. These grains were carefully checked and avoided during the EPMA and LA-ICP-MS analyses. Melts quenched to clear glasses in most of the runs, with several exceptions conducted at high pressures (2–3 GPa), for which the melts formed dendritic mineral aggregates upon quenching. In these cases, large apertures were used for the EPMA and LA-ICP-MS analyses.

Major and trace element compositions of the run products are reported in Tables S1–2. Mg# of olivines ranged from 79 to 96. Compositions of opxs ($Wo_{2.5\text{-}5.2}En_{78.3\text{-}92.1}Fs_{5.0\text{-}16.7}$, Mg# = 82–95, tetrahedrally coordinated $Al^T$ = 0.07–0.17) and cpxs ($Wo_{33.8\text{-}47.3}En_{45.0\text{-}61.5}Fs_{2.6\text{-}14.2}$, Mg# = 78–95, tetrahedrally coordinated $Al^T$=0.10–0.28) varied moderately (Figure 3). Pyroxene compositions in this study are comparable to those of the depleted MORB mantle (DMM) recommended by Workman and Hart (2005), but clearly higher in $Al_2O_3$ and $Al^T$ than those crystalized at 1 atm (literature data, Tables S4 e–f). The deficient of $Al_2O_3$ and $Al^T$ in pyroxenes synthesized at 1atm might be caused by plagioclase crystallization, which leads to low $Al_2O_3$ content in the coexisting melts. It is also possible that pressure exerts an effect on $Al_2O_3$ and $Al^T$ contents in the pyroxenes.

Spinels were mainly composed of solid-solutions of $FeCr_2O_4$-$FeFe_2O_4$-$MgAl_2O_4$ (chromite-magnetite-spinel) with minor $TiO_2$ (< 1.0 wt %). $Cr^{\#}$ (molar Cr/(Al+Cr)) of the spinels ranged from 4.1 to 52.5. Garnets were formed at high pressures (2.0-3.0 GPa) and plagioclase were formed in the 0.5–1.0 GPa and $H_2O$-poor experiments. The melts are typically basaltic, containing 2.0–10 wt% $H_2O$, according to the mass difference between EPMA total and 100%. All the quenched melts were homogenous in composition. When normalizing the EPMA total to 100%, $SiO_2$ contents in the quenched melts ranged from 44.8 wt% to 53.2 wt% and MgO contents ranged from 7.1 wt% to 16.3 wt%.

4.2 Chemical and $fO_2$ equilibrium

To avoid the notoriously sluggish equilibration of crystalline starting materials, we used the amorphous starting materials in this study. Experimental durations in this study were extended relative to the previous phase-equilibrium study with similar compositions (Pichavant et al., 2002). Approach to chemical equilibrium in our experiments can be demonstrated by the following evidences: (1) homogeneity of major and trace element contents in the run products (Tables S1–2; incomplete equilibrium (i.e. zoning) was observed in some cpx grains in several runs but these grains were avoided for trace element analyses); (2) constant $Fe^{2+}$-Mg exchange Kd values for olivine-melt (0.35 ± 0.05, Table S1 b and Figure S1), in accord with previous studies (Hirose and Kawamoto, 1995; Gaetani and Grove, 1998; Falloon and Danyushevsky, 2000); and (3) regular variations of mineral/melt $D_V$, $D_{Sc}$ and $D_{Ti}$ with experimental conditions, as shown in Figures 5 and 6 and Figure S4.

Oxygen fugacity equilibration is governed by complex interactions as described in section 2.3. During an experiment, the initial $fO_2$ gradient across the capsule wall leads to H diffusion into or out of the capsule until $fH_2$ reaches equilibrium, after which, $fO_2$ and Fe exchange between capsule and sample charge also reach equilibrium. H diffusion through the capsule wall will cause changes of $fO_2$ and $H_2O$ activity in the charge due to the reaction $H_2+0.5O_2 = H_2O$. Meanwhile, $Fe^{3+}$/ $Fe^{2+}$ in the charge will be modulated by the reaction $Fe_2O_3 = FeO+0.5O_2$ to match the $fO_2$, and Fe loss/gain will take place according to the reaction $FeO = Fe+0.5O_2$ in response to the H diffusion-driven $fO_2$ change.

In this study, the starting compositions were homogenized at 1500 ℃ in air (log $fO_2$ = -0.68) and thus has $Fe^{3+}/Fe_T$ = 0.596, calculated from the algorithm of Kress and Carmichael (1991). All the runs (with three exceptions) showed some Fe-loss (Table 2), indicating iron reduction regardless of the capsule alloy compositions. Iron reduction and subsequent alloying with capsules produce $O_2$ by the reactions $Fe_2O_3 = 2FeO+0.5O_2$ and $FeO = Fe+0.5O_2$, resulting in an increase in the experimental $fO_2$. However, the resultant $O_2$ will react with $H_2$ to form $H_2O$, and final $fO_2$ of the charge is controlled by the H diffusion equilibrium. This mechanism is indicated by an increase of $H_2O$ content in most of our experiments, and by the reduction (from air $fO_2$ to experimental $fO_2$) of the samples during experiments (Table 2). Six out of 38 runs showed $H_2O$ loss during experiments, which may have been caused by an additional process such as carbon permeability. For these runs, the graphite furnaces may have been in contact with the capsules, allowing carbon to diffuse from the graphite furnaces into the capsules and to react with oxygen ($C + O_2 = CO_2$). Reaction between carbon and oxygen will consume $O_2$ and cause subsequent $H_2O$ decomposition ($H_2O = H_2+0.5O_2$), leading to an overall decrease in $H_2O$ content of the experiments.

Over the past decades, petrologists have conducted a number of piston-cylinder experiments using AuPd and AuPdFe alloy capsules as sample containers, and demonstrated that short durations (8–12 h) are sufficient for Fe exchange and $fO_2$ equilibrium (e.g., Jakobsson, 2012; Kägi et al., 2005). Our experiments (20–50 h) exceeded these durations, and $fO_2$ equilibrium is indicated by two lines of evidences: (1) The nearly constant $Fe^{2+}$-Mg exchange Kd values between olivine and melt (0.35 ± 0.05, Table S1b and Figure S1) demonstrate that the $Fe^{2+}$-Mg exchange between olivine and melt reached equilibrium; (2) Homogeneous Fe contents in the quenched melt and capsule wall for each of the runs (Table S1 h) indicate Fe exchange equilibrium between capsule and melt. We analyzed Fe contents across the capsule walls in two representative runs (bw-23 and bw-37, data in Table S1i). As

shown in Figure S2, no significant diffusion gradient was detected in these two runs, indicating that Fe diffusion equilibrium was approached in our experiments.

4.3 Determination of experimental $fO_2$

There are three approaches that can be used to determine the experimental $fO_2$. The most direct approach is to analyze $Fe^{3+}/Fe_T$ of the quenched melt by Mössbauer spectroscopy or X-Ray Near Edge Spectrometry (XANES). However, hampered by the size of the melt pools, the Mössbauer spectroscopy technique is excluded from this study. It`s also a challenge to apply the XANES technique to hydrous glasses (Cottrell et al., 2018) or reduced samples with very low $Fe^{3+}$ content (Sorbadere et al., 2018). Another widely used approach is to calculate $fO_2$ by the mineral oxybarometers (olivine-opx-spinel). Two forms of this approach have been developed: one is based on a thermodynamic formulation (Mattioli and Wood, 1988; Wood and Virgo, 1989) and the other is based on a semi-empirical equation (Ballhaus et al., 1991). The former was developed based on the thermodynamic data presented in Bohlen et al. (1980) and Myers and Eugster (1983), and requires accurate determination of the magnetite activity in spinel. To obtain accurate values for magnetite activity, a correction method was introduced by Wood and Virgo (1989) and revisited recently by Davis et al. (2017). However, magnetite activity in spinel, which strongly affects the calculated $fO_2$, is model-dependent (e.g., Davis and Cottrell, 2018; O`Neill and Wall, 1987), and so far no universally-accepted spinel model has been developed (Davis and Cottrell, 2018). The semi-empirical equation developed by Ballhaus et al. (1991) was based on a series of high pressure experiments. This equation has been used to determine $fO_2$ values of both experimental and natural samples (Evans et al., 2012; Jugo, 2005; Jugo et al., 2005). Ballhaus et al. (1991)'s calibration requires neither the opx composition nor magnetite activity in spinel. It was claimed that the standard deviation of this calibration is ± 0.4 log units at $fO_2$ above FMQ, and the absent of opx would rarely cause an error in excess of 0.2 log units (Ballhaus et al., 1991). Using gas-mixing furnace, Davis and Cottrell (2018) equilibrated olivine-opx-spinel-melt at 1atm, 1225 ℃. They determined $fO_2$ values of these experiments from µ-XANES analyses of the quenched melt, and then compared these values with $fO_2$ calculated from the thermodynamically-derived olivine-opx-spinel oxybarometer. Their study paves the way for us to compare the two mineral oxybarometers. In Figure 4 a, we compare the $fO_2$ values obtained from the µ-XANES technique and mineral oxybarometers using the data in Davis and Cottrell (2018). The results exhibit good consistency between the µ-XANES technique and mineral oxybarometers and demonstrate the accuracy of both the semi-empirical equation (Ballhaus et al., 1991) and the thermodynamic formulation (Wood and Virgo, 1989; Davis et al., 2017). Because Davis and Cottrell (2018)`s experiments were performed at 1 atm, the results in Figure 4 a also confirm the consistency between mineral oxybarometers and gas-mixing furnace $fO_2$.

The third approach that can be used to estimate $fO_2$s of the run products is the Fe-alloy redox sensors. Fe content of the noble metal in equilibrium with silicate melt is a function of the ambient $fO_2$. Barr and Grove (2010) calibrated the equilibrium constant for AuPdFe alloys coexisting with Fe-bearing silicate melts and developed the AuPdFe alloy-melt $fO_2$ sensor, which was shown to be accurate at least at $fO_2$ below FMQ (Sorbadere et al., 2018). Using both the AuPdFe sensor and semi-empirical olivine-opx-spinel oxybarometer (Ballhaus et al., 1991), we calculated $fO_2$ values in eight of our experiments, in which olivine, opx and spinel coexisted. Direct comparison between the AuPdFe sensor and mineral oxybarometer are exhibited in Figure 4 b, where the high consistency between these two methods ($y=0.94x$, $r^2=0.96$) corroborates the accuracy of the AuPdFe sensor and validates the robustness of these

two techniques. Here, we further demonstrate the consistency among AuPdFe sensor, mineral oxybarometer and gas-mixing furnace. As mentioned above (Figure 4 b), the AuPdFe sensor and olivine-opx-spinel oxybarometer agree with each other at our reduced high pressure experiments. The agreement between these two approaches at 1 atm can be demonstrated as follows: $fO_2$ of the FMQ buffer can be calculated by $\log fO_2 = -25096/T+8.74+0.11*(P-1)/T$ (equation A) (Frost 1991); while, for the AuPdFe sensor, the ambient $fO_2$ is modulated by reaction $2Fe(alloy) + O_2 = 2FeO(melt)$ and $fO_2$ of this reaction can be calculated by $\log fO_2 = -27215/T+6.57+0.056*(P-1)/T$ (equation B) (Frost 1991). In both equation (A) and (B), T is temperature in K and P is pressure in bar. Therefore, we can calculate pressure effect on the AuPdFe sensor by subtracting equation (A) from (B). The result demonstrates that at a given temperature, e.g. 1250 $^oC$, $\log fO_2$ of AuPdFe sensor varies by -0.355/GPa relative to FMQ buffer. For the case of olivine-spinel oxybarometer, we can calculated pressure effect using the coefficient of pressure term (-400·P/T, Ballhaus 1991). The result shows that at 1250 $^oC$, $\log fO_2$ of olivine-opx-spinel oxybarometer vaires -0.263/GPa relative to FMQ. Therefore, the difference between AuPdFe sensor and olivine-opx-spinel oxybarometer barely exceeds 0.1 log units (-0.263-(-0.355)) per GPa and such difference remains almost constant within the temperature range of this study (1150–1350 $^oC$). Therefore, we believe that the AuPdFe sensor and mineral oxybarometer are consistent at 1atm. Recently, Davis and Cottrell. (2018) confirmed the $fO_2$ consistency between olivine-opx-spinel oxybarometer and gas-mixing furnace at 1 atm. Therefore, in conjunction with our ratiocination above, we can conclude with confidence that $fO_2$ recorded by olivine-opx-spinel oxybarometer, AuPdFe sensor and controlled by gas-mixing furnace are consistent with each other. Consequently, it is safe to make a direct comparison of $D_V$ values collected in this study.

In this study, we used AuPd or AuPdFe alloys as sample containers and these alloys facilitated utilizing the AuPdFe sensor at reduced conditions. Some of the alloy capsules contain 2 wt% Cu. This amount of Cu has an influence less than 2 % relative on Fe activity of the alloys and is thus considered to be negligible in the $fO_2$ calculations. We have calculated experimental $fO_2$s (Table 2) using both the semi-empirical equation (Ballhaus et al., 1991) and the AuPdFe sensor (Barr and Grove, 2010). As pointed out, the olivine-opx-spinel oxybarometer has small errors at oxidized conditions, but large errors at reduced conditions due to the large uncertainties associated with spinel $Fe^{3+}$ contents (Ballhaus et al., 1991); whereas the AuPdFe sensor is more precise at reduced conditions (Barr and Grove, 2010), but has large errors at oxidized conditions due to the very low Fe contents in alloy capsules (Sorbadere et al., 2018). Therefore, to ensure the most accurate $fO_2$ values were utilized, we adopt $fO_2$ values obtained from the olivine-opx-spinel oxybarometer at oxidized conditions ($fO_2$ > FMQ) and those obtained from the AuPdFe sensor at reduced conditions ($fO_2$ < FMQ). The calculated and selected (adopted) $fO_2$ values are reported in Table 2.

4.4 Mineral/melt partition coefficients

Mineral/melt D-values of the FRTEs are reported in Tables S3 a–f. D-values for other elements will be reported elsewhere. Trace element contents in our experimental charges are lower than or comparable to those in previous studies (Canil, 1997; Davis et al., 2013; Le Roux et al., 2011), which were verified to obey Henry's law. The original purpose of this study was to accurately determine the D-values of V, Ti, Sc, Zn and Fe between mantle minerals and basaltic melts. However, we found that significant Zn-loss occurred at reduced conditions (Figure S3). This effect may degrade the quality of $D_{Zn}$ values and prevents us from further discussing Zn-Fe systematics in tracking mantle redox states. Thus, we focus here on the partitioning of V, Sc and Ti. The results show that partitioning of these elements

is independent of melt $H_2O$ content. For example, runs HMB-9 and HMB-10 have the same T (1350 $^oC$) and P (1.0 GPa), similar $fO_2$ ($\Delta$FMQ $\simeq$ 0.0) and phase assemblages and compositions (olivine, spinel and melt), but different melt $H_2O$ contents (6.8 - 8.9 wt%). D-values of V, Sc and Ti for olivine/melt, and V and Ti for spinel/melt between these two runs are the same within errors. No effect of $H_2O$ on $D_V$ for olivine in a hydrous basaltic system has also been reported in a recent study (Shishkina et al., 2018). The D-values are functions of experimental conditions and phase compositions as stated as follows.

4.4.1 $D_V$

$D_V$ values for olivine, opx, cpx, spinel and garnet were 0.005–0.186, 0.13–4.0, 0.20–4.5, 0.96–25 and 0.13–3.15, respectively, under our experimental conditions (Tables S3 a–e). No significant effect of pressure on $D_V$ was observed, in agreement with previous studies (Canil, 1999; Canil and Fedortchouk, 2000; Mallmann and O'Neill, 2009; Mallmann and O'Neill, 2013), except for the study of Li (2018). Li (2018) conducted experiments using graphite-lined $Pt_{95}Rh_5$ capsules at various pressures and temperatures and assumed, by buffering at C-$CO_2$, $fO_2$ was constant in his charges. However, as pointed out by previous studies (Frost and Wood, 1997; Wood et al., 1990), $fO_2$ of the C-$CO_2$ buffer is strongly pressure-dependent, such that Li's (2018) assumption seems to be problematic.

A strong $fO_2$-dependence of $D_V$ values for olivine, opx, cpx and spinel was observed in this study (Figures 5 and 6), consistent with previous studies (Canil, 1997; Canil, 1999; Canil and Fedortchouk, 2000; Laubier et al., 2014; Mallmann et al., 2009). It has been verified that $Al^T$ (Al in the tetrahedron-coordinated site) in pyroxenes has a positive effect on the $D_V$, $D_{Sc}$ and $D_{Ti}$ (Wood and Blundy, 2001; Lo Cascio et al., 2008; Davis et al., 2013), and $Cr^{\#}$ [Cr/(Cr+Al)] exerts a positive effect on $D_V$ for spinel (Canil, 1999). We also observed a clear effect of $Al^T$ in pyroxenes on the $D_V$. For example, at the same P (2.0 GPa), T (1350 $^oC$) and $fO_2$ ($\Delta$FMQ $\simeq$ -0.85), $D_V$ (0.61) for opx/melt in run HMB-12 (opx $Al^T$ = 0.07) is clearly lower than that ($D_V$ = 1.15; opx $Al^T$ = 0.13) in run HMB-14. In addition, we note that, at similar $fO_2$ and temperature, $D_V$ values for opx and cpx in our experiments are higher than those obtained from 1 atm experiments (Figures 5 and 6). This phenomenon can be explained by the higher $Al^T$ content in pyroxenes crystallized from our high pressure experiments (see Figure 3).

Mineral/melt trace element D-values are expected to increase monotonically with reciprocal temperature given other conditions remain constant (Wood and Blundy, 2001). However, such an effect of temperature on $D_V$ for the mantle minerals has not yet been addressed, except for olivine (Mallmann et al., 2013). To clearly address the effect of temperature, $D_V$ data from this study and the literatures were used together (Table S4 a). We culled subsets of experiments with similar $fO_2$s (variation within < $\pm$ 0.25 log units) to show the temperature effect on $D_V$. In Figure 5 a, b and c, there are two groups of data for olivine/melt at $fO_2$ ($\Delta$FMQ) = -1.87 $\pm$ 0.13 and $\simeq$ 0.0 (a), two groups of data for opx/melt at $fO_2$ ($\Delta$FMQ) = -1.07 $\pm$ 0.22 and 0.10 $\pm$ 0.10 (b), and three groups of data for cpx/melt at $fO_2$ ($\Delta$FMQ) = -1.12 $\pm$ 0.27, 0.24 $\pm$ 0.05 and 2.98 $\pm$ 0.21 (c). These three panels (a, b and c) show clearly that $D_V$ at each $fO_2$ group decreases with increasing temperature for olivine, opx and cpx. We used two groups of data, respectively at 1180–1200 $^oC$ and 1300 $^oC$ to determine the effect of temperature on spinel/melt $D_V$. It shows in Figure 5 d that at a given $fO_2$, $D_V$ values for spinel were generally higher at 1180–1200 $^oC$ than those at 1300 $^oC$, although the significant effect of $Cr^{\#}$ makes the temperature effect less clear. All of these results indeed indicate a negative effect of temperature on the V partitioning.

4.4.2 $D_{Sc}$

$D_{Sc}$ values for olivine, opx, cpx and garnet were 0.10–0.20, 0.61–2.15, 1.40–4.70 and 4.01–7.56, respectively, under our experimental conditions (Tables S3 a–f). $D_{Sc}$ for spinel was not obtained due to the extremely low Sc contents in this phase. These results indicate that Sc is highly incompatible in olivine and spinel, incompatible to compatible in opx and cpx and highly compatible in garnet, in agreement with the results of Davis et al. (2013). $D_{Sc}$ values for both opx and cpx decrease with increasing pressure (Figure S4). Temperature could also cause a decrease of $D_{Sc}$ for these two phases, but such an effect appears to be secondary relative to pressure. $D_{Sc}$ for olivine does not significantly change with experimental conditions. We recommended $D_{Sc}$= 0.12 for olivine from the average of this study and $D_{Sc}$ = 0.06 for spinel from Davis et al. (2013) for the partial melting modelling presented in sections 5.2 and 5.3.

4.4.3 $D_{Ti}$

Titanium is highly incompatible in nearly all the mantle phases. $D_{Ti}$ values for olivine, opx, cpx, spinel and garnet are only slightly pressure and temperature dependent and are < 0.01, < 0.2, < 0.4, < 0.5 and < 0.3, respectively, at the mantle melting pressures of ≥ 1.0 GPa (Tables S3 a–f and Figure S4). The high incompatibility of Ti in mantle minerals makes it an excellent proxy for the degree of mantle melting (Prytulak and Elliott, 2007). For the mantle melting modelling presented in sections 5.2 and 5.3, we recommended $D_{Ti}$ = 0.008 for olivine and $D_{Ti}$ = 0.30 for spinel.

4.5 Multiple linear regressions for $D_V$, $D_{Sc}$ and $D_{Ti}$

Statistical deconvolution method was used to quantitatively evaluate the effect of each variable ($fO_2$, T, P, composition of mineral or melt) on the $D_V$, $D_{Sc}$ and $D_{Ti}$ between mantle minerals and basaltic melts. D-values from this study together with published data were used for multiple linear regressions of $D_V$ for olivine, opx, cpx and spinel, and $D_{Sc}$ and $D_{Ti}$ for opx and cpx as functions of $fO_2$, T, P and phase compositions (see the data filtration criteria in Text S1–3 and data sources in Tables S4 a–g). For each of the variables, the statistically significant P-value was confined to < 0.05. The linear regressions analysis yield the following results:

(1) $\log(D_V^{ol/melt}) = -2.30(\pm0.28) - 0.258(\pm0.006)\Delta FMQ + 1871(\pm398)/T - 0.24(\pm0.03)NBO/Tot$ (n = 195, $r^2 = 0.90$)

(2) $\log(D_V^{opx/melt}) = -4.61(\pm0.58) - 0.198(\pm0.014)\Delta FMQ + 5981(\pm871)/T + 4.48(\pm0.52)Al^T$ ($n = 40, r^2 = 0.91$)

(3) $\log(D_V^{cpx/melt}) = -4.24(\pm0.63) - 0.267(\pm0.012)\Delta FMQ + 5717(\pm1016)/T + 3.64(\pm0.62)Al^T$ ($n = 40, r^2 = 0.94$)

(4) $\log(D_V^{sp/melt}) = -1.09(\pm0.76) - 0.186(\pm0.013)\Delta FMQ + 2447(\pm1128)/T + 0.004(\pm0.001)Cr^{\#}$ ($n$=59, $r^2 = 0.82$)

(5) $\log(D_{Sc}^{opx/melt}) = 3.31(\pm0.23) - 73(\pm22)P/T - 0.038(\pm0.002)Mg^{\#}$ ($n = 52, r^2 = 0.83$)

(6) $\log(D_{Sc}^{cpx/melt}) = -1.51(\pm0.30) + 2342(\pm498)/T - 160(\pm30)P/T + 2.44(\pm0.40)Al^T$ ($n = 66, r^2 = 0.79$)

(7) $\log(D_{Ti}^{opx/melt}) = -3.46(\pm0.21) + 3852(\pm320)/T - 92(\pm30)P/T + 0.87(\pm0.30)Al^T$ ($n = 38, r^2 = 0.93$)

(8) $\log(D_{Ti}^{cpx/melt}) = -1.48(\pm0.21) + 1154(\pm353)/T - 235(\pm25)P/T + 2.53(\pm0.31)Al^T$ ($n = 72, r^2 = 0.88$)

In equations 1–8, T is temperature in Kelvin; P is pressure in GPa; ΔFMQ is the $fO_2$ difference between experimental $fO_2$ and FMQ buffer at P and T. NBO/Tot = $(4\cdot X_T - 2\cdot X_O)/X_T$ refers to melt polymerization degree, in which $X_T$ and $X_O$ are respectively the atomic proportions of tetrahedron-coordinated cations and oxygen (Mysen, 2014). $Al^T$ is Al

in tetrahedrally-coordinated site (atom per formula unit) in opx or cpx. $Cr^{\#}$ equals to Cr/(Al+Cr) in spinel on a molar basis. Details of the fitting processes are described in Text S1–3.

The high $r^2$ values (0.79 to 0.94) for equations 1–8 and good agreements between experimental and calculated D-values (Figure S5) demonstrate the reliability of these parameterizations. The results show that $D_V$ values for olivine, opx, cpx and spinel (equations 1–4 and Figure 6) decrease with increasing $fO_2$ and temperature, especially for opx and cpx; melt composition has a minor effect on the olivine $D_V$; $Al^T$ has a positive effect on the $D_V$ for opx and cpx; and $Cr^{\#}$ has a positive effect on the $D_V$ for spinel. $D_{SC}$ and $D_{Ti}$ for opx and cpx (equations 5–8) decrease with increasing pressure and temperature; $Al^T$ has a positive effect on $D_{Sc}$ and $D_{Ti}$ for pyroxenes; and $Mg^{\#}$ has a minor negative effect on $D_{Sc}$ for opx. These statistical results are consistent with the experimental observations as stated in sections 4.4, and further confirms no effect of pressure on $D_V$ as pointed out in section 4.4.1.

Using the fitted equations (2-3 and 5-8), we further examined the temperature dependencies of $D_V$, $D_{Sc}$, $D_{Ti}$, $D_V/D_{Sc}$ and $D_V/D_{Ti}$ for opx and cpx. The results (Figure 7) show that at given $fO_2$ and pressure, $D_V$, $D_{Sc}$, $D_{Ti}$, $D_V/D_{Sc}$ and $D_V/D_{Ti}$ for pyroxenes all decrease with increasing temperature. In particular, the decreases of both $D_V/D_{Sc}$ and $D_V/D_{Ti}$ with increasing temperature indicate that the temperature-dependency of $D_V$ values are greater than that of $D_{Sc}$ and $D_{Ti}$. The greater temperature-dependency of $D_V$ suggest that for mantle partial melting at lower temperatures, V tends to partition into residual minerals more easily, relative to Sc and Ti. Therefore, at a given $fO_2$, mantle-derived melts formed at lower temperatures should have lower V/Sc and V/Ti ratios than those formed at higher temperatures. Furthermore, if primitive arc basalts and MORBs are formed at different temperatures, their similar V/Sc or V/Ti ratios should indicate the difference in $fO_2$ of their mantle sources.

## 5. Discussion

### 5.1 Pressures and temperatures of primitive basalts

As documented in sections 4.1–3, temperature and pressure exert effects on D values of V, Sc and Ti between mantle minerals and basaltic melt. Therefore, the P-T conditions for the generation of basaltic magmas are prerequisite for the estimation of mantle $fO_2$ using elemental ratios such as V/Sc and V/Ti. Compositions of basalts provide a window into the P-T conditions of their generations (e.g., Herzberg et al., 2007; Putirka et al., 2007). We collected major and trace element contents of primitive arc basalts from GeoROC (http://georoc.mpch-mainz.gwdg.de). For primitive MORBs, the data were collected from literatures (Gale et al., 2013; Jenner and O'Neill, 2012; Shimizu et al., 2016) and PetDB (http://www. earthchem.org). The compiled primitive basalts data (MgO > 8.0 wt%) were then filtered to exclude unreasonable data (criteria in Text S2). The filtered data (Tables S5–6) include 668 arc samples from 26 arc segments and 299 MORB samples (Pacific Ocean: n=161, Indian Ocean: n=16 and Atlantic Ocean: n=122). Although all the samples have MgO > 8.0 wt%, fractionation of minerals was inevitable during magma storage and ascent. To obtain primary melts in equilibrium with mantle peridotite, a reversal fractionation correction was performed. It was believed that olivine should be the only early crystallization phase at MgO ≥ 8.0 wt% (e.g., Dasgupta et al., 2010). We thus corrected the compositions of the samples only by addition of olivine. During the corrections, olivine was added at a step of 0.1% until the melt is in equilibrium with $Fo_{90}$. For the corrections of MORBs, the initial $Fe^{3+}/Fe_T$ was set at 0.138 (Zhang et al., 2018). For arc basalts, the initial $Fe^{3+}/Fe_T$ was set at 0.20, which is in the $Fe^{3+}/Fe_T$ range of primitive arc basalts [0.18 to 0.22 in Kelley and

Cottrell (2012)]. In the corrections of MORBs and arc basalts, $Fe^{3+}$ was treated as a perfect incompatible element and thus $Fe^{3+}/Fe_T$ ratio in the melt decreases with the addition of olivine. A constant $Fe^{2+}$-Mg exchange coefficient (Kd) of 0.30 between olivine and melt (Roeder, 1970) was used in the corrections. V, Sc and Ti contents in the melt were also corrected by dilution of the original contents according to olivine fraction added into the samples, assuming complete incompatibility of these elements. The corrected major element composition of each sample was then employed to calculate the P-T conditions for melt generation using the melt-thermobarometer of Lee et al. (2009). Before the P and T calculations, water content of the melt must be well constrained. For MORBs, mean water content of 0.2 wt% (Li et al., 2017) was used in the T and P calculations. For primary arc basalts, water content determined from olivine ($Mg^{\#} > 86$) hosted melt inclusions ranges from 2 to 6 wt%, with an average of ~4 wt% (Plank et al., 2013; Wallace, 2005; Zimmer et al., 2010). Here we calculated the T and P conditions of arc basalts assuming water content of 2, 4 and 6 wt %, respectively. In this way, we obtained temperature and pressure for each sample at a given $H_2O$ content. The calculated temperatures and pressures for all the MORBs and arc basalts are presented in Figure 8. As shown in Figure 8, temperatures and pressures for the MORBs are in the ranges of 1300 ℃–1420 ℃ and 0.7–1.8 GPa, respectively. For the arc basalts, the pressure ranges from 0.6 to 2.1 GPa, and the temperature ranges from 1200 to 1350 ℃, 1175 to 1325 ℃ and 1150 to1280 ℃ at 2, 4 and 6 wt% $H_2O$ contents, respectively. These results indicate that the equilibrium pressures between primitive melts and mantle are similar for arc basalts and MORBs, but the equilibrium temperatures of arc basalts are generally lower than those of MORBs due to their higher $H_2O$ contents.

5.2 Similar V/Sc or V/Ti ratios between arc basalts and MORBs do not mean similar $fO_2$s in their mantle sources

V, Sc and Ti have been demonstrated to be immobile during the dehydration of subducted oceanic crust (Green and Adam, 2003) and sediment (Spandler et al., 2007). These elements were also assumed to be immobile during slab melting given their very high mineral/melt D-values ($D_V$ and $D_{Sc}$ between garnet/cpx and rhyolitic melt greater than 10 (Sisson, 1991); $D_V$ and $D_{Ti}$ for rutile/felsic melt greater than 100 (Foley et al., 2000; Xiong et al., 2005)). In some circumstances, carbonate melts may be able to transport and reset V, Sc and Ti contents of the mantle (Woodland et al., 2018), but their amount and distribution should be limited in subduction zones. Thus V, Sc and Ti abundances in arc mantle and oceanic mantle should be generally similar (Lee et al., 2005; Mallmann and O'Neill, 2009). Shervais (1982) also claimed that V/Ti ratio remains unchanged during alteration and metasomatic processes, and thus proposed that V/Ti ratio in ophiolites can be used as a discriminant of mantle $fO_2$.

Here, we evaluated whether similar V/Sc or V/Ti ratios in primitive mantle magmas do indeed reflect the $fO_2$ similarity in their sources when the effect of temperature on D-values is considered. We assume that pressure and residual mineral compositions are similar during the partial melting of oceanic and arc mantle. To evaluate redox states of the oceanic and arc mantle, we performed partial melting modelling. The spinel lherzolite mineral assemblage (57% olivine, 28% opx, 13% cpx, and 2% spinel) and compositions (opx $Al^T = 0.15$, cpx $Al^T = 0.17$ and spinel $Cr^{\#} = 10.7$) from Workman and Hart (2005) and trace element contents (V = 79 ppm, Sc = 16.3 ppm, and Ti = 798 ppm) from Salters and Stracke (2004), were used as the initial mantle composition. In the modelling, the melting reactions from Falloon et al. (2008) and Gaetani and Grove, (1998) were used for anhydrous MORB mantle melting and hydrous arc mantle melting, respectively. Thus, the amount of each residual mineral changes

with the progress of partial melting, and then the bulk D-value for a certain element varies accordingly. Near fractional melting and batch melting models were employed for oceanic and arc mantle melting, respectively. During the anhydrous melting at a given pressure, degree of melting is a function of temperature. Therefore, for the generation of MORBs, we can calculate the melting degree and temperature using a melt productivity of 0.23/℃ for lherozlite and 0.14/℃ for harzburgite, respectively (Falloon et al., 2008). We assumed that the initial melt was formed at 1300 ℃ (taken from Figure 8) and then the degree of melting reasonably reaches 20% at 1400 ℃. In this way, the melting temperature at each melt fraction can be estimated and the bulk D-values for V, Sc and Ti can be calculated from the estimated T and residual mineral assemblages. For the case of arc basalts, the situation is more complicated because degree of melting increases with initial $H_2O$ content at given temperature. We tentatively used a melt productivity of 0.23/℃ (lherozlite melting) and assumed the initial melting occurred at 1200 ℃ and the partial melting ceased at 1310 $^{o}$C. At each melt fraction (or temperature), equations 1–8 were used to calculate $D_V$ values for olivine, opx, cpx and spinel and $D_{Sc}$ and $D_{Ti}$ values for opx and cpx. Combining the calculated and recommended D-values with the residual mineral assemblages, we can estimate, at given $fO_2$, the bulk D-values for V, Sc and Ti at each melting degree (Recommended D-values: $D_{Ti}$ = 0.008 for olivine; $D_{Ti}$ = 0.30 for spinel; $D_{Sc}$ = 0.12 for olivine and $D_{Sc}$ = 0.06 for spinel). Using the bulk D-values at each degree of melting, we modelled $fO_2$ isopleths for the V/Ti-Ti and V/Sc-Ti systematics during the generations of MORBs and arc basalts at 1.0 GPa (Figure 9). We also performed calculations to assess the effect of mantle heterogeneity on the modelled $fO_2$ isopleths, using uncertainties of 7% for V, 12% for Ti and 13% for Sc (Salters and Stracke, 2004). Finally, we projected the fractionation-corrected V/Ti-Ti and V/Sc-Ti of primitive MORBs and arc basalts onto the calculated $fO_2$ isopleths in Figure 9. We can find from this figure that: (1) The results obtained from V/Ti–Ti and V/Sc–Ti systematics are in agreement with each other; (2) The $fO_2$s of MORBs are around FMQ, whereas those of arc basalts are generally higher than FMQ, indicating that arc mantle is generally more oxidized than oceanic mantle; (3) At a given degree of melting, similar V/Sc or V/Ti ratios between arc basalts and MORBs indicate higher $fO_2$ at arc mantle due to the lower melting temperatures. Details for the partial melting modeling are reported in Text S3.

5.3 $fO_2$ estimations of oceanic mantle and arc mantle.

We found that during mantle partial melting, Sc can be compatible or incompatible depending on P-T conditions and residual mineral assemblages, such as the amount of cpx ± garnet (section 4.2), whereas Ti is highly incompatible in all mantle minerals and its content in the partial melt will monotonically decrease with increasing melt fraction. Therefore, relative to Sc, Ti is a superior proxy for the degree of melting. Here we estimated $fO_2$ of each primitive basalt using V-Ti systematics following two steps.

Firstly, we determined the degree of melting and the residual mineral assemblage for each sample by matching the modelled Ti contents to the fractionation-corrected sample Ti contents. The difference between the modelled and corrected Ti contents for each sample was set at < 3‰. More than 94% of the samples conformed to this rule and only these samples were used in the subsequent $fO_2$ estimation. In fact, this difference is a trade-off. If we set a very small difference, we can estimate the partial melting degree with a high precision, however, the amount of matched samples will shrink. If a big difference is used, the amount of matched samples will increase, but the precision will degrade. Titanium in primitive basalts (Tables S5–6) ranges from 3000 to 9000 ppm. Less than 3‰ means the difference

between modelled and natural sample Ti contents varies between 9 to 27 ppm and the estimated melting degree has an error < 0.3% absolute.

Secondly, degree of melting, residual mineral assemblage, phase composition, temperature and pressure were used to estimate the $fO_2$ of each sample. During the calculations, oxygen fugacity (and thus bulk $D_V$) was varied until the modelled V contents matched the sample V contents. Specifically, $fO_2$ varied from FMQ-2.5 to FMQ+4 at a step of 0.001 log unit until the difference between the modelled and sample V contents was within 5‰. Calculated results for all the samples using V-Ti systematics are shown in Figure 10. Details of the $fO_2$ estimation routines are given in Tables S9–10. As shown in Figure 10, the $fO_2$s for MORBs and their mantle sources range from FMQ-1.7 to FMQ+0.5 with a median at FMQ-0.03, which are in excellent agreement with the previous results of Ballhaus (1993), Lee et al. (2005) and Zhang et al. (2018). The calculated $fO_2$s for arc basalts depend on the bulk $D_V$, which is in turn dependent on the calculated temperatures at the given $H_2O$ content. For the 2 wt% $H_2O$ case (Figure 10 a), the $fO_2$ median of arc basalts is 0.45 log units higher than that of MORBs (FMQ+0.42 vs. FMQ-0.03) with ~55% of the arc samples overlapping the $fO_2$ range of MORBs. At the $H_2O$ content of 4 wt% (Figure 10 b), the $fO_2$ median of arc basalts is 0.85 log units higher than that of MORBs (FMQ+0.82 vs. FMQ-0.03) with only ~27% of the samples overlapping the $fO_2$ range of MORBs. For the 6 wt% $H_2O$ case, the $fO_2$ median of arc basalts is 1.2 log units higher than that of MORBs (FMQ+1.16 vs. FMQ-0.03) with ~13% of the samples overlapping the $fO_2$ range of MORBs (Figure 10 c). These results indicate that the mantle sources for arc basalts are generally higher in $fO_2$ than MORB sources, though overlap exists. Given that primitive arc basalts have an average of 4 wt% $H_2O$ (Plank et al., 2013), we believe that the calculated results with 4 wt% $H_2O$ are representative of the general $fO_2$ range in arc mantle. That is, global arc mantle is 0.9 log units higher in $fO_2$ than oceanic mantle on average. This conclusion is in contrast to the results of previous V/Sc and Zn/Fe studies (Lee et al., 2005; 2010), but is in general consistent with the results of $Fe^{3+}/Fe_T$ studies on arc basalts (Brounce et al., 2014, 2015; Carmichael, 1991; Kelley and Cottrell, 2009, 2012) and the results of mineralogy study on arc mantle xenolith (Parkinson and Arculus, 1999).

5.4 Fluid influx and oxidation of arc mantle

A generally positive correlation between $fO_2$ and fluid input has been observed in primitive arc basalts in previous studies (Bénard et al., 2018; Brounce et al., 2014, 2015; Debret et al., 2016; Evans and Tomkins, 2011; Evans, 2012; Kelley and Cottrell, 2009; Pons et al., 2016; Rielli et al., 2017), and thus fluid influx was proposed as the cause of mantle wedge oxidization. V/Ti ratios in ophiolites (Shervais, 1982) and basalts (Woodhead et al., 1993 and this study) can be used to record $fO_2$ in their mantle sources. Therefore, here we use V/Ti to represent oxidation extent and Ba/La to represent fluid flux to further test, from a global perspective, the correlation between $fO_2$ and fluid input. Barium (Ba) readily partitions into aqueous fluid and melt, whereas lanthanum (La) is fluid immobile but melt mobile. Thus, the Ba/La ratio will isolate the fluid signatures from the melts and can be used as a proxy for fluid input (Brounce et al., 2014, 2015; Kelley and Cottrell, 2009). In the data compiled from 26 arcs globally (Table S8), 16 arcs each contain ≥ 10 samples that have paired V/Ti and Ba/La data. We plotted V/Ti vs. Ba/La ratios for basalts from these arcs in Figure S6. Among the 16 arcs, 11 arcs (New Hebridges, Mariana, Liguria, Honshu, Mexican, Tonga, Scotia, Kamchatka, Bismarck, Luzon, and Cascades) show good positive correlations ($r^2 > 0.50$) between V/Ti and Ba/La. We then plotted Ba/La vs. Ti (ppm) and V/Ti vs. Ba/La for primitive basalts from these 11 arcs, together with MORBs for comparison (Figure 11).

As shown in Figure 11 a, with increasing degree of melting (i.e. the decrease of Ti content in basalt), the Ba/La ratios are invariable in MORBs but increase in arc basalts. This phenomenon suggests that fluid input has caused an increase in the degree of melting by lowering solidus of the mantle wedge. Figure 11 b shows that V/Ti ratios of the arc basalts generally overlap those of the MORBs when subduction input is limited (Ba/La ≤ 12; the MORB range). However, the V/Ti ratios increases considerably with enhanced subduction input (Ba/La > 12), indicating that oxidation of the arc mantle is indeed intimately related to fluid input, as has been demonstrated by previous studies (e.g., Brounce et al., 2014, 2015; Kelley and Cottrell, 2009).

## 6. Summary

We performed high pressure experiments to determine the D-values of FRTEs between mantle minerals and basaltic melts. Combining our results with published data, the effects of $fO_2$, P, T and phase compositions on $D_V$, $D_{Sc}$ and $D_{Ti}$ were quantitatively assessed by multiple linear regressions. We found that in addition to $fO_2$, temperature also exerts an important influence on the $D_V$. In particular, the temperature-dependency of $D_V$ exceeds its effect on $D_{Ti}$ and $D_{Sc}$, indicating that at given $fO_2$, melt formed at lower temperature should have lower V/Sc or V/Ti ratios. Because primitive arc basalts are generally formed at temperatures lower than that of MORBs, the similar V/Sc or V/Ti ratios between them should indeed indicate the higher $fO_2$ in arc mantle. We then estimated $fO_2$s of the magmas and their mantle sources by partial melting modelling, considering temperature difference between primitive arc basalts and MORBs and its effect on D-values. The results reveal that the arc mantle is generally 0.9 log units higher in $fO_2$ than the oceanic mantle, providing new evidence for relatively oxidized arc mantle. Our conclusions offer a global perspective on the oxidation state of arc mantle and do not exclude the presence of locally reduced arc mantle (e.g., Song et al., 2009) and the possible oxidization during magmatic evolution (e.g., Tang et al., 2018).

**Acknowledgements**

We thank P.J. Lin and J.H. Zhu for electron microprobe assistance; F.Y. Wang for LA-ICPMS assistance. We acknowledge Maryjo Brounce and two anonymous reviewers for their thorough review of this manuscript. We also thank Stephen Parman for the handling of this manuscript. In addition, the constructive comments from Fred A. Davis, V. Le Roux, and Katherine A. Kelley for a previously unpublished version also improved this manuscript significantly. This work was supported by the Strategic Priority Research Program (XDB18000000), Key Research Program of Frontier Sciences (QYZDJ-SSW-DQC012) of the CAS, and the GIG135 Project (GIG135PY201601) to X.L.X and NSFC (41573053) to X. Liu. The authors declare that they have no competing interests. This is contribution No. IS-#xxx from GIGCAS. All data supporting the conclusions of this paper can be found in the cited references, tables, supporting information and in Mendeley Dataset, DOI: 10.17632/933fg2h4zs.1 or http://dx.doi.org/10.17632/933fg2h4zs.1

## References

Aeolus Lee, C.T., Leeman, W.P., Canil, D., & Li, Z.-X.A. (2005). Similar V/Sc Systematics in MORB and Arc Basalts: Implications for the Oxygen Fugacities of their Mantle Source Regions. Journal of Petrology 46, 2313-2336.

Bénard, A., Klimm, K., Woodland, A.B., Arculus, R.J., Wilke, M., Botcharnikov, R.E., Shimizu, N., Nebel, O., Rivard, C., & Ionov, D.A. (2018). Oxidising agents in sub-arc mantle melts link slab devolatilisation and arc magmas. Nature Communications 9.

Bézos, A., & Humler, E. (2005). The Fe3+/ΣFe ratios of MORB glasses and their implications for mantle melting. Geochimica et Cosmochimica Acta 69, 711-725.

Ballhaus, C. (1993). Redox States of Lithospheric and Asthenospheric Upper-Mantle. Contributions to Mineralogy and Petrology 114, 331-348.

Ballhaus, C., Berry, R.F., & Green, D.H. (1990). Oxygen fugacity controls in the Earth`s upper mantle. Nature 348, 4.

Ballhaus, C., Berry, R.F., & Green, D.H. (1991). High pressure experimental calibration of the olivine-orthopyroxene-spinel oxygen geobarometer: implications for the oxidation state of the upper mantle. Contributions to Mineralogy and Petrology.

Barr, J.A., & Grove, T.L. (2010). AuPdFe ternary solution model and applications to understanding the fO2 of hydrous, high-pressure experiments. Contributions to Mineralogy and Petrology 160, 631-643.

Berry, A.J., Stewart, G.A., O'Neill, H.S.C., Mallmann, G., & Mosselmans, J.F.W. (2018). A re-assessment of the oxidation state of iron in MORB glasses. Earth and Planetary Science Letters 483, 114-123.

Blundy, J.D., Robinson, J.A.C., & Wood, B.J. (1998). Heavy REE are compatible in clinopyroxene on the spinel lherzolite solidus. Earth and Planetary Science Letters 160, 493-504.

Bohlen, S.R., Essene, E.J., & Boettcher, A.L. (1980). Reinvestigation and Application of Olivine-Quartz-Orthopyroxene Barometry. Earth and Planetary Science Letters 47, 1-10.

Brounce, M., Kelley, K.A., Cottrell, E., & Reagan, M.K. (2015). Temporal evolution of mantle wedge oxygen fugacity during subduction initiation. Geology 43, 775-778.

Brounce, M.N., Kelley, K.A., & Cottrell, E. (2014). Variations in Fe3+/ Fe of Mariana Arc Basalts and Mantle Wedge fO2. Journal of Petrology 55, 2513-2536.

Canil, D. (1997). Vanadium partitioning and the oxidation state of Archaean komatite magmas. Nature.

Canil, D. (1999). Vanadium partitioning between orthopyroxene, spinel and silicate melt and the redox states of mantle source regions for primary magmas. Geochimica Et Cosmochimica Acta 63, 557-572.

Canil, D., & Fedortchouk, Y. (2000). Clinopyroxene-liquid partitioning for vanadium and the oxygen fugacity during formation of cratonic and oceanic mantle lithosphere. Journal of Geophysical Research-Solid Earth 105, 26003-26016.

Carmichael, I.S.E. (1991). The redox states of basic and silicic magmas: a reflection of their source regions? Contributions to Mineralogy and Petrology 106, 13.

Chou, I.-M. (1987). Oxygen buffer and hydrogen sensor techniques at elevated pressures and temperatures.

Christie, D.M., Carmichael, I.S.E., & Langmuir, C.H. (1986). Oxidation states of mid-ocean ridge basalt glasses. Earth and Planetary Science Letters 79, 397-411.

Cottrell, E., & Kelley, K.A. (2011). The oxidation state of Fe in MORB glasses and the oxygen fugacity of the upper mantle. Earth and Planetary Science Letters 305, 270-282.

Cottrell, E., Lanzirotti, A., Mysen, B., Birner, S., Kelley, K.A., & Botcharnikov, R., Davis, F.A., Newville, M. (2018). A Mössbauer-based XANES calibration for hydrous basalt glasses reveals radiation-induced oxidation of Fe. American Mineralogist 103, 489-501.

Dasgupta, R., Jackson, M.G., & Lee, C.-T.A. (2010). Major element chemistry of ocean island basalts — Conditions of mantle melting and heterogeneity of mantle source. Earth and Planetary Science Letters 289, 377-392.

Davis, F.A., & Cottrell, E. (2018). Experimental investigation of basalt and peridotite oxybarometers: Implications for spinel thermodynamic models and Fe3+ compatibility during generation of upper mantle melts. American Mineralogist 103, 1056-1067.

Davis, F.A., Cottrell, E., Birner, S.K., Warren, J.M., & Lopez, O.G. (2017). Revisiting the electron microprobe method of spinel-olivine-orthopyroxene oxybarometry applied to spinel peridotites. American Mineralogist 102, 421-435.

Davis, F.A., Humayun, M., Hirschmann, M.M., & Cooper, R.S. (2013). Experimentally determined mineral/melt partitioning of first-row transition elements (FRTE) during partial melting of peridotite at 3GPa. Geochimica et Cosmochimica Acta 104, 232-260.

Debret, B., Millet, M.A., Pons, M.L., Bouilhol, P., Inglis, E., & Williams, H. (2016). Isotopic evidence for iron mobility during subduction. Geology 44, 215-218.

Evans, K.A. (2012). The redox budget of subduction zones. Earth-Science Reviews 113, 11-32.

Evans, K.A., Elburg, M.A., & Kamenetsky, V.S. (2012). Oxidation state of subarc mantle. Geology 40, 783-786.

Evans, K.A., & Tomkins, A.G. (2011). The relationship between subduction zone redox budget and arc magma fertility. Earth and Planetary Science Letters 308, 401-409.

Falloon, T.J., & Danyushevsky, L.V. (2000). Melting of refractory mantle at 1.5, 2 and 2.5 GPa under, anhydrous and H2O-undersaturated conditions: Implications for the petrogenesis of high-Ca boninites and the influence of subduction components on mantle melting. Journal of Petrology 41, 257-283.

Falloon, T.J., Green, D.H., Danyushevsky, L.V., & McNeill, A.W. (2008). The Composition of Near-solidus Partial Melts of Fertile Peridotite at 1 and 1.5 GPa: Implications for the Petrogenesis of MORB. Journal of Petrology 49, 591-613.

Fialin, M., Outrequin, M., & Staub, P.F. (1997). A new tool to treat peak overlaps in electron-probe microanalysis of rare-earth-element L-series X-rays. Eur J Mineral 9, 965-968.

Foley, S.F., Barth, M.G., & Jenner, G.A. (2000). Rutile/melt partition coefficients for trace elements and an assessment of the influence of rutile on the trace element characteristics of subduction zone magmas. Geochimica Et Cosmochimica Acta 64, 933-938.

Frost, B.R. (1991). Introduction to Oxygen Fugacity and Its Petrologic Importance. Rev Mineral 25, 1-9.

Frost, D.J., & McCammon, C.A. (2008). The Redox State of Earth's Mantle. Annual Review of Earth and Planetary Sciences 36, 389-420.

Frost, D.J., & Wood, B.J. (1997). Experimental measurements of the fugacity of CO2 and graphite/diamond stability from 35 to 77 kbar at 925 to 1650 degrees C. Geochimica Et Cosmochimica Acta 61, 1565-1574.

Gaetani, G.A., & Grove, T.L. (1998). The influence of water on melting of mantle peridotite. Contributions to Mineralogy and Petrology 131, 323-346.

Gale, A., Dalton, C.A., Langmuir, C.H., Su, Y., & Schilling, J.-G. (2013). The mean composition of ocean ridge basalts. Geochemistry, Geophysics, Geosystems 14, 489-518.

Green, T.H., & Adam, J. (2003). Experimentally-determined trace element characteristics of aqueous fluid from partially dehydrated mafic oceanic crust at 3.0 GPa, 650-700°C. Eur J Mineral 15, 815-830.

Hamada, M., & Fujii, T. (2007). Experimental constraints on the effects of pressure and H2O on the fractional crystallization of high-Mg island arc basalt. Contributions to Mineralogy and Petrology 155, 767-790.

Herzberg, C., Asimow, P.D., Arndt, N., Niu, Y., Lesher, C.M., Fitton, J.G., Cheadle, M.J., & Saunders, A.D. (2007). Temperatures in ambient mantle and plumes: Constraints from basalts, picrites, and komatiites. Geochemistry, Geophysics, Geosystems 8, n/a-n/a.

Hirose, K., & Kawamoto, T. (1995). Hydrous partial melting of lherzolite at 1 GPa: The effect of H2O on the genesis of basaltic magmas. Earth and Planetary Science Letters 133, 11.

J.Wood, B., & D.Blundy, J. (2001). The effect of cation charge on crystal-melt partitioning of trace elements.

Jackson, C.M., Cottrell, E., & Kelley, K.A. (2010). Mineral-melt partitioning of V and Sc at arcs: implications for mantle wedge oxygen fugacity. American Geophysical Union, Fall Meeting 2010 #V11F-01.

Jakobsson, S. (2012). Oxygen fugacity control in piston-cylinder experiments. Contributions to Mineralogy and Petrology 164, 397-406.

Jenner, F.E., & O'Neill, H.S.C. (2012). Analysis of 60 elements in 616 ocean floor basaltic glasses. Geochemistry, Geophysics, Geosystems 13, n/a-n/a.

Jugo, P.J. (2005). An Experimental Study of the Sulfur Content in Basaltic Melts Saturated with Immiscible Sulfide or Sulfate Liquids at 1300 oC and 1.0 GPa. Journal of Petrology 46, 783-798.

Jugo, P.J., Luth, R.W., & Richards, J.P. (2005). Experimental data on the speciation of sulfur as a function of oxygen fugacity in basaltic melts. Geochimica et Cosmochimica Acta 69, 497-503.

Kägi, R., Muntener, O., Ulmer, P., & Ottolini, L. (2005). Piston-cylinder experiments on H2O undersaturated Fe-bearing systems: An experimental setup approaching fO2 conditions of natural calc-alkaline magmas. American Mineralogist 90, 708-717.

Kelley, K.A., & Cottrell, E. (2009). Water and the oxidation state of subduction zone magmas. Science 325, 605-607.

Kelley, K.A., & Cottrell, E. (2012). The influence of magmatic differentiation on the oxidation state of Fe in a basaltic arc magma. Earth and Planetary Science Letters 329-330, 109-121.

Kress, V.C., & Carmichael, I.S.E. (1991). The compressibility of silicate liquids containing Fe2O3 and the effect composition, temperature, oxygen fugacity and pressure on their redox states Contributions to Mineralogy and Petrology 108, 11.

Kump, L.R., Kasting, J.F., & Barley, M.E. (2001). Rise of atmosphere oxygen and the "upside-down" Archean mantle. Geochem Geophy Geosy 2, 10.

Laubier, M., Grove, T.L., & Langmuir, C.H. (2014). Trace element mineral/melt partitioning for basaltic and basaltic andesitic melts: An experimental and laser ICP-MS study with application to the oxidation state of mantle source regions. Earth and Planetary Science Letters 392, 265-278.

Le Roux, V., Dasgupta, R., & Lee, C.T.A. (2011). Mineralogical heterogeneities in the Earth's mantle: Constraints from Mn, Co, Ni and Zn partitioning during partial melting. Earth and Planetary Science Letters 307, 395-408.

Lee, C.-T.A., Luffi, P., Plank, T., Dalton, H., & Leeman, W.P. (2009). Constraints on the depths and temperatures of basaltic magma generation on Earth and other terrestrial planets using new thermobarometers for mafic magmas. Earth and Planetary Science Letters 279, 20-33.

Lee, C.T., Luffi, P., Le Roux, V., Dasgupta, R., Albarede, F., & Leeman, W.P. (2010). The redox state of arc mantle using Zn/Fe systematics. Nature 468, 681-685.

Li, W., Jin, Z., Li, H., & Tao, C. (2017). High water content in primitive mid-ocean ridge basalt from Southwest Indian Ridge (51.56ºE): Implications for recycled hydrous component in the mantle. Journal of Earth Science 28, 411-421.

Li, Y. (2018). Temperature and pressure effects on the partitioning of V and Sc between clinopyroxene and silicate melt: Implications for mantle oxygen fugacity. American Mineralogist 103, 819-823.

Liu, X., Xiong, X., Audétat, A., & Li, Y. (2015). Partitioning of Cu between mafic minerals, Fe-Ti oxides and intermediate to felsic melts. Geochimica et Cosmochimica Acta.

Liu, X., Xiong, X., Audétat, A., Li, Y., Song, M., Li, L., Sun, W., & Ding, X. (2014). Partitioning of copper between olivine, orthopyroxene, clinopyroxene, spinel, garnet and silicate melts at upper mantle conditions. Geochimica et Cosmochimica Acta 125, 1-22.

Lo Cascio, M., Liang, Y., & Shimizu, N., Hess, P.C. (2008). An experimental study of the grain-scale processes of peridotite melting: implications for major and trace element distribution during equilibrium and disequilibrium melting. Contributions to Mineralogy and Petrology 156, 87-102.

Luth, R.W. (1989). Natural versus experimental control of oxidation state: Effects on the composition and speciation of C-O-H fluids. American Mineralogist 74, 8.

Mallmann, G., & O'Neill, H.S.C. (2009). The Crystal/Melt Partitioning of V during Mantle Melting as a Function of Oxygen Fugacity Compared with some other Elements (Al, P, Ca, Sc, Ti, Cr, Fe, Ga, Y, Zr and Nb). Journal of Petrology 50, 1765-1794.

Mallmann, G., & O'Neill, H.S.C. (2013). Calibration of an Empirical Thermometer and Oxybarometer based on the Partitioning of Sc, Y and V between Olivine and Silicate Melt. Journal of Petrology 54, 933-949.

Mallmann, G., O'Neill, H.S.C., & Klemme, S. (2009). Heterogeneous distribution of phosphorus in olivine from otherwise well-equilibrated spinel peridotite xenoliths and its implications for the mantle geochemistry of lithium. Contributions to Mineralogy and Petrology 158, 485-504.

Matjuschkin, V., Brooker, R.A., Tattitch, B., Blundy, J.D., & Stamper, C.C. (2015). Control and monitoring of oxygen fugacity in piston cylinder experiments. Contributions to Mineralogy and Petrology 169.

Mattioli, G.S., & Wood, B.J. (1988). Magnetite activities across the MgAI204 -Fe304 spinel join, with application to thermobarometric estimates of upper mantle oxygen fugacity. Contributions to Mineralogy and Petrology 98, 15.

Myers, J., & Eugster, H.P. (1983). The System Fe-Si-O: Oxygen Buffer Calibrations to 1,500 K. Contributions to Mineralogy and Petrology 82, 16.

Mysen, B. (2014). Water-melt interaction in hydrous magmatic systems at high temperature and pressure. Progress in Earth and Planetary Science 1, 18.

Niu, Y., & Green, D.H. (2018). The petrological control on the lithosphere-asthenosphere boundary (LAB) beneath ocean basins. Earth-Science Reviews 185, 301-307.

O`Neill, H.S.C., & Wall, V.J. (1987). The olivine-orthopyroxene-spinel oxygen geobarometer, the nickel precipation curve, and the oxygen fugacity of the Earth`s upper mantle. Journal of Petrology 28, 23.

Papike, J.J., Burger, P.V., Bell, A.S., Le, L., Shearer, C.K., Sutton, S.R., Jones, J., & Newville, M. (2013). Developing vanadium valence state oxybarometers (spinel-melt, olivine-melt, spinel-olivine) and V/(Cr plus Al) partitioning (spinet-melt) for martian olivine-phyric basalts. American Mineralogist 98, 2193-2196.

Parkinson, I.J., & Arculus, R.J. (1999). The redox state of subduction zones: insights from arc-peridotites. Chemical Geology 160, 409-423.

Pertermann, M., Hirschmann, M.M., Hametner, K., Günther, D., & Schmidt, M.W. (2004). Experimental determination of trace element partitioning between garnet and silica-rich liquid during anhydrous partial melting of MORB-like eclogite. Geochemistry, Geophysics, Geosystems 5, n/a-n/a.

Pichavant, M., Mysen, B.O., & Macdonald, R. (2002). Source and H2O content of high-MgO magmas in island arc settings: An experimental study of a primitive calc-alkaline basalt from St. Vincent, Lesser Antilles arc. Geochimica Et Cosmochimica Acta 66, 2193-2209.

Plank, T., Kelley, K.A., Zimmer, M.M., Hauri, E.H., & Wallace, P.J. (2013). Why do mafic arc magmas contain ~4 wt% water on average? Earth and Planetary Science Letters 364, 168-179.

Pons, M.L., Debret, B., Bouilhol, P., Delacour, A., & Williams, H. (2016). Zinc isotope evidence for sulfate-rich fluid transfer across subduction zones. Nat Commun 7, 13794.

Prytulak, J., & Elliott, T. (2007). TiO2 enrichment in ocean island basalts. Earth and Planetary Science Letters 263, 388-403.

Putirka, K.D., Perfit, M., Ryerson, F.J., & Jackson, M.G. (2007). Ambient and excess mantle temperatures, olivine thermometry, and active vs. passive upwelling. Chemical Geology 241, 177-206.

Rielli, A., Tomkins, A.G., Nebel, O., Brugger, J., Etschmann, B., Zhong, R., Yaxley, G.M., & Paterson, D. (2017). Evidence of sub-arc mantle oxidation by sulphur and carbon. Geochemical Perspectives Letters, 124-132.

Righter, K., Sutton, S.R., Newville, M., Lei, L., Schwandt, C.S., Uchida, H., Lavina, B., & Downs, R.T. (2006). An experimental study of the oxidation state of vanadium in spinel and basaltic melt with implications for the origin of planetary basalt. American Mineralogist 91, 1643-1656.

Roeder, P.L. (1970). Olivine-Liquid Equilibrium. Contributions to Mineralogy and Petrology 29, 15.

Rohrbach, A., & Schmidt, M.W. (2011). Redox freezing and melting in the Earth's deep mantle resulting from carbon-iron redox coupling. Nature 472, 209-212.

Salters, V.J.M., & Stracke, A. (2004). Composition of the depleted mantle. Geochemistry, Geophysics, Geosystems 5, n/a-n/a.

Shervais, J.W. (1982). Ti-V plots and the petrogenesis of modern and ophiolitic lavas. Earth and Planetary Science Letters 59, 18.

Shimizu, K., Saal, A.E., Myers, C.E., Nagle, A.N., Hauri, E.H., Forsyth, D.W., Kamenetsky, V.S., & Niu, Y. (2016). Two-component mantle melting-mixing model for the generation of mid-ocean ridge basalts: Implications for the volatile content of the Pacific upper mantle. Geochimica et Cosmochimica Acta 176, 44-80.

Shishkina, T.A., Portnyagin, M.V., Botcharnikov, R.E., Almeev, R.R., Simonyan, A.V., Garbebe-Schonberg, D., Schuth, S., Oeser, M., & Holtz, F. (2018). Experimental calibration and implications of olivine-melt vanadium oxybarometry for hydrous basaltic arc magmas. American Mineralogist 103, 369-383.

Sisson, T.W., (1991). Pyroxene-High Silica Rhyolite Trace-Element Partition-Coefficients Measured by Ion Microprobe. Geochimica Et Cosmochimica Acta 55, 1575-1585.

Song, S., Su, L., Niu, Y., Lai, Y., & Zhang, L. (2009). CH4 inclusions in orogenic harzburgite: Evidence for reduced slab fluids and implication for redox melting in mantle wedge. Geochimica et Cosmochimica Acta 73, 1737-1754.

Sorbadere, F., Laurenz, V., Frost, D.J., Wenz, M., Rosenthal, A., McCammon, C., & Rivard, C. (2018). The behaviour of ferric iron during partial melting of peridotite. Geochimica et Cosmochimica Acta.

Spandler, C., Mavrogenes, J., & Hermann, J. (2007). Experimental constraints on element mobility from subducted sediments using high-P synthetic fluid/melt inclusions. Chemical Geology 239, 228-249.

Tang, M., Erdman, M., Eldridge, G., & Lee, C.-T.A. (2018). The redox "filter" beneath magmatic orogens and the formation of continental crust. Science Advances 4, 7.

Toplis, M.J., & Corgne, A. (2002). An experimental study of element partitioning between magnetite, clinopyroxene and iron-bearing silicate liquids with particular emphasis on vanadium. Contributions to Mineralogy and Petrology 144, 22-37.

Wallace, P.J. (2005). Volatiles in subduction zone magmas: concentrations and fluxes based on melt inclusion and volcanic gas data. Journal of Volcanology and Geothermal Research 140, 217-240.

Wood, B.J., & Blundy, J.D. (2001). The effect of cation charge on crystal-melt partitioning of trace elements. Earth and Planetary Science Letters 188, 59-71.

Wood, B.J., Bryndzia, L.T., & Johnson, K.E. (1990). Mantle oxidation state and its relationship to tectonic environment and fluid speciation. Science 248, 337-345.

Wood, B.J., & Virgo, D. (1989). Upper mantle oxidation state: Ferric iron contents of lherzolite spinels by 57Fe Mössbauer spectroscopy and resultant oxygen fugacities. Geochimica et Cosmochimica Acta 53, 1277-1291.

Woodhead, J., Eggins, S., & Gamble, J. (1993). High field strength and transition element systematics in island arc and back-arc basin basalts" evidence for multi-phase melt extraction and a depleted mantle wedge. Earth and Planetary Science Letters 114, 14.

Woodland, A.B., Uenver-Thiele, L., & Seitz, H.M. (2018). Influence of metasomatism on vanadium-based redox proxies for mantle peridotite. Geochemical Perspectives Letters, 11-16.

Workman, R.K., & Hart, S.R. (2005). Major and trace element composition of the depleted MORB mantle (DMM). Earth and Planetary Science Letters 231, 53-72.

Xiong, X.L., Adam, J., & Green, T.H. (2005). Rutile stability and rutile/melt HFSE partitioning during partial melting of hydrous basalt: Implications for TTG genesis. Chemical Geology 218, 339-359.

Zhang, H.L., Cottrell, E., Solheid, P.A., Kelley, K.A., & Hirschmann, M.M. (2018). Determination of Fe3+ /ΣFe of XANES basaltic glass standards by Mössbauer spectroscopy and its application to the oxidation state of iron in MORB. Chemical Geology 479, 166-175.

Zimmer, M.M., Plank, T., Hauri, E.H., Yogodzinski, G.M., Stelling, P., Larsen, J., Singer, B., Jicha, B., Mandeville, C., & Nye, C.J. (2010). The Role of Water in Generating the Calc-alkaline Trend: New Volatile Data for Aleutian Magmas and a New Tholeiitic Index. Journal of Petrology 51, 2411-2444

Table 1. Major and trace element compositions of the starting materials.

| . | SM 1 | 1σ | SM 2 | SM 3 | S-KLB-1 |
|---|---|---|---|---|---|
| SiO2 | 46.71 | 0.23 | 47.11 | 46.81 | 45.08 |
| TiO2 | 0.97 | 0.03 | 0.83 | 0.73 | 0.11 |
| Al2O3 | 15.49 | 0.13 | 13.59 | 12.10 | 3.53 |
| FeO | 9.30 | 0.19 | 9.25 | 9.10 | 8.24 |
| MnO | 0.22 | 0.02 | 0.18 | 0.16 | 0.00 |
| MgO | 11.43 | 0.13 | 16.62 | 20.02 | 39.63 |
| CaO | 11.07 | 0.11 | 9.82 | 8.82 | 3.09 |
| Na2O | 2.34 | 0.05 | 2.01 | 1.76 | 0.30 |
| K2O | 0.41 | 0.01 | 0.35 | 0.30 | 0.02 |
| Cr2O3 | 0.20 | 0.02 | 0.17 | 0.14 | |
| NiO | 0.05 | 0.02 | 0.05 | 0.04 | |
| P2O5 | 0.03 | 0.00 | 0.03 | 0.02 | |
| Total | 98.23 | 0.58 | 100.0 | 100.0 | 100. 0 |
| Sc | 98 | 1 | 700 | 700 | |
| V | 224 | 2 | 700 | 700 | |
| Cr | 1172 | 15 | 938 | 820 | |
| Co | 204 | 1 | 163 | 143 | |
| Ni | 572 | 3 | 458 | 400 | |
| Cu | 281 | 2 | 224 | 196 | |
| Zn | 955 | 9 | 764 | 669 | |
| Cs | 78 | 1 | 63 | 55 | |

The major elements in wt % for SM1 were determined by EMPA (n=10), and the trace elements in µg/g were determined by LA-ICP-MS (n=4). SM 2 and SM 3 are mixtures of SM 1 and the synthesized KLB-1 composition with ratios of 4.7:1 and 2.5:1, respectively. Additionally, scandium and vanadium are added to SM 2 and SM 3 at around 700 ppm. All Fe is reported as FeO.

Table 2. Summary of the experimental conditions, run products and $fO_2$

| Run No. | P (Gpa) | T (°C) | Startinga material | Duration (Hours) | Sample capsule | Run products (wt %)[b] Ol | Sp | Opx | Cpx | Gt | Pl | melt | $\Sigma R^2$ [c] | $H_2O$ loss[d] wt % | Fe losse (relative) | $fO_2$ (ΔFMQ)[f] Ol-Sp | $fO_2$ (ΔFMQ)[g] AuPdFe | Selected $fO_2$[h] ( Δ FMQ) |
|---|---|---|---|---|---|---|---|---|---|---|---|---|---|---|---|---|---|---|
| bw-12 | 1.0 | 1180 | 6+SM 1 | 50 | $Au_{80}Pd_{17}Cu_2Fe_1$ | 4.9 | 2.7 | 3.0 | 28.0 | | 5.3 | 56.0 | 0.4 | -6.5 | 1.1 | -0.92 | -1.29 | -1.29 |
| bw-14* | 1.0 | 1180 | 5+SM 1 | 50 | $Au_{80}Pd_{17}Cu_2Fe_1$ | 7.5 | 2.3 | 3.0 | 21.2 | | 10.0 | 56.0 | 0.3 | -5.5 | 12.0 | -1.05 | -1.09 | -1.09 |
| bw-15* | 1.0 | 1180 | 5+SM 1 | 50 | $Au_{80}Pd_{17}Cu_2Fe_1$ | | 2.5 | 13.6 | 4.6 | | 1.0 | 78.2 | 0.5 | 0.7 | -4.7 | | -1.44 | -1.44 |
| bw-23 | 1.0 | 1200 | 5+SM 1 | 50 | $Au_{80}Pd_{17}Cu_2Fe_1$ | 8.0 | 3.0 | | 11.0 | | 2.0 | 76.0 | 1.6 | -2.6 | -5.9 | -2.10 | -1.37 | -1.37 |
| bw-25 | 1.0 | 1200 | 5+SM 1 | 50 | $Au_{80}Pd_{17}Cu_2Fe_1$ | 1.0 | tr | | | | | 99.0 | 1.8 | 9.3 | -67.5 | | -2.72 | -2.72 |
| bw-32* | 1.0 | 1200 | 5+SM 1 | 20.5 | $Au_{80}Pd_{20}$ | | 3.0 | 7.0 | 23.0 | | 2.0 | 65.0 | 1.5 | -1.4 | -7.1 | | -0.16 | -0.16 |
| bw-33 | 1.0 | 1200 | 5+SM 1 | 20.5 | $Au_{80}Pd_{17}Cu_2Fe_1$ | 5.0 | 2.0 | 12.4 | 11.0 | | 13.3 | 56.3 | 0.9 | -2.3 | -11.0 | -2.25 | -1.63 | -1.63 |
| bw-34 | 1.0 | 1200 | 5+SM 1 | 20.5 | $Au_{80}Pd_{17}Cu_2Fe_1$ | 8.0 | 2.0 | | 1.0 | | tr | 89.0 | 0.1 | 1.5 | -15.5 | -2.57 | -1.56 | -1.56 |
| bw-35 | 2.0 | 1200 | 5+SM 1 | 35 | $Au_{80}Pd_{20}$ | | | 4.0 | 15.0 | 16.0 | | 65.0 | 1.0 | 1.9 | -61.9 | | -2.09 | -2.09 |
| bw-37 | 2.0 | 1150 | 5+SM 1 | 30 | $Au_{80}Pd_{17}Cu_2Fe_1$ | tr | tr | 10.0 | | | | 90.0 | 9.9 | 3.9 | -21.6 | -2.55 | -2.84 | -2.84 |
| bw-44 | 1.0 | 1180 | 5+SM 1 | 38 | $Au_{75}Pd_{25}$ | tr | 0.7 | | | | | 92.8 | 0.6 | 3.9 | -6.7 | 2.34 | 1.69 | 2.34 |
| bw-48 | 1.0 | 1180 | 4+SM 1 | 22 | $Au_{75}Pd_{25}$ | 4.0 | 6.0 | | 24.0 | | | 66.0 | 2.9 | -2.1 | -18.3 | 1.25 | 0.60 | 1.25 |
| bw-49 | 1.0 | 1180 | 4+SM 1 | 22 | $Au_{75}Pd_{25}$ | 1.6 | 4.6 | | | | | 93.8 | 0.8 | 1.6 | -6.8 | 2.75 | 1.89 | 2.75 |
| bw-50 | 1.0 | 1180 | 4+SM 1 | 24 | $Au_{75}Pd_{25}$ | 4.8 | tr | | | | | 95.2 | 1.7 | 2.9 | -14.6 | 3.32 | 1.66 | 3.32 |
| bw-51 | 1.0 | 1180 | 4+SM 1 | 24 | $Au_{75}Pd_{25}$ | 4.8 | 0.3 | | | | | 94.9 | 1.2 | 3.6 | -12.8 | 3.57 | 1.92 | 3.57 |
| bw-54 | 2.0 | 1180 | 4+SM 1 | 22 | $Au_{75}Pd_{25}$ | | 7.9 | 1.2 | 41.6 | | | 49.3 | 0.3 | 2.0 | -5.2 | | 1.09 | |
| bw-55 | 2.0 | 1180 | 4+SM 1 | 22 | $Au_{75}Pd_{25}$ | | 4.7 | 0.3 | 27.5 | | | 67.5 | 0.2 | 4.0 | -4.5 | | 0.99 | |
| bw-56 | 3.0 | 1230 | 6+SM 1 | 22 | $Au_{75}Pd_{25}$ | | | | 30.1 | 15.3 | | 54.5 | 1.7 | 1.1 | -5.7 | | | |
| bw-57 | 3.0 | 1230 | 5+SM 1 | 22 | $Au_{75}Pd_{25}$ | | | | | 22.6 | | 77.4 | 5.5 | 5.5 | -7.6 | | | |
| bw-58 | 0.5 | 1180 | 0+SM 1 | 22 | $Au_{75}Pd_{25}$ | 7.5 | 4.6 | | 11.5 | | 1.0 | 75.6 | 0.0 | 2.4 | -10.2 | 1.93 | 1.09 | 1.93 |
| bw-59 | 0.5 | 1180 | 0+SM 1 | 22 | $Au_{75}Pd_{25}$ | 8.3 | 4.7 | | 12.5 | | 5.0 | 69.5 | 0.0 | 2.8 | -14.0 | 1.57 | 0.78 | 1.57 |
| bw-60 | 0.5 | 1190 | 0+SM 1 | 24 | $Au_{75}Pd_{25}$ | 9.0 | 3.4 | | 6.3 | | 5.0 | 76.3 | 0.0 | 4.3 | -30.0 | 0.74 | 0.78 | 0.74 |
| bw-61 | 0.5 | 1190 | 0+SM 1 | 24 | $Au_{75}Pd_{25}$ | 10.7 | 2.0 | | 5.8 | | 9.0 | 72.7 | 0.0 | 5.3 | -30.9 | 1.34 | 0.07 | 1.34 |
| bw-64 | 2.0 | 1200 | 5+SM 1 | 20 | $Au_{75}Pd_{25}$ | | 3.8 | | 26.2 | 6.3 | | 63.8 | 0.1 | 2.0 | -0.7 | | 1.02 | |
| 907-2b | 1.5 | 1320 | 0+SM 1 | 25 | $Au_{75}Pd_{25}$ | | | | 21.0 | | | 79.0 | 15.3 | 1.6 | -74.9 | | | |
| 910-5b | 1.0 | 1180 | 3+SM 1 | 40 | $Au_{80}Pd_{17}Cu_2Fe_1$ | 7.0 | tr | | tr | | | 93.0 | 7.6 | 1.4 | 55.6 | 0.38 | -0.68 | -0.68 |
| HMB-1 | 1.0 | 1250 | 3+SM 2 | 30.5 | $Au_{75}Pd_{25}$ | 14.6 | tr | | 14.1 | | | 71.3 | 1.9 | 4.5 | -68.9 | | -0.94 | -0.94 |
| HMB-2 | 1.0 | 1250 | 3+SM 2 | 30.5 | $Au_{75}Pd_{24.5}Fe_{0.5}$ | 16.7 | 0.8 | | 14.0 | | | 68.6 | 0.1 | 3.8 | -70.6 | -1.67 | -1.82 | -1.82 |
| HMB-3 | 1.0 | 1250 | 3+SM 2 | 30.5 | $Au_{75}Pd_{23.5}Fe_{1.5}$ | 16.7 | tr | | 12.2 | | | 71.1 | 7.9 | 3.8 | -13.8 | -0.95 | -0.91 | -0.91 |
| HMB-6 | 1.5 | 1250 | 3+SM 2 | 38 | $Au_{75}Pd_{25}$ | tr | 1.3 | 22.3 | 15.6 | | | 60.8 | 3.8 | 7.6 | -45.4 | 0.29 | 0.26 | 0.29 |
| HMB-7 | 1.5 | 1250 | 3+SM 2 | 38 | $Au_{75}Pd_{24.5}Fe_{0.5}$ | tr | 2.2 | 25.1 | 21.3 | | | 51.4 | 2.5 | 3.8 | -23.8 | -0.09 | -0.04 | -0.04 |
| HMB-8 | 1.5 | 1250 | 3+SM 2 | 38 | $Au_{75}Pd_{23.5}Fe_{1.5}$ | tr | 2.5 | 25.7 | 23.4 | | | 48.4 | 7.9 | 3.3 | -1.0 | -0.36 | -0.49 | -0.49 |
| HMB-9 | 1.0 | 1350 | 1.5+SM 3 | 20.5 | $Au_{75}Pd_{25}$ | 18.3 | tr | | | | | 81.7 | 1.0 | 7.1 | -58.8 | 0.18 | 0.30 | 0.08 |
| HMB-10 | 1.0 | 1350 | 1.5+SM 3 | 20.5 | $Au_{75}Pd_{24.5}Fe_{0.5}$ | 19.1 | tr | | | | | 80.9 | 2.5 | 4.9 | -33.0 | -0.07 | 0.15 | 0.05 |
| HMB-11 | 1.0 | 1350 | 1.5+SM 3 | 20.5 | $Au_{75}Pd_{23.5}Fe_{1.5}$ | 21.2 | tr | | | | | 78.8 | 6.9 | 4.5 | -6.0 | -0.62 | -0.39 | -0.39 |
| HMB-12 | 2.0 | 1350 | 1.5+SM 3 | 20.5 | $Au_{75}Pd_{25}$ | 2.4 | | 20.5 | 2.9 | | | 74.2 | 1.7 | 9.3 | -67.3 | | -0.85 | -0.85 |
| HMB-13 | 2.0 | 1350 | 1.5+SM 3 | 20.5 | $Au_{75}Pd_{24.5}Fe_{0.5}$ | 1.1 | | 27.6 | 7.1 | | | 64.2 | 2.6 | 8.7 | -44.9 | | -0.71 | -0.71 |
| HMB-14 | 2.0 | 1350 | 1.5+SM 3 | 20.5 | $Au_{75}Pd_{23.5}Fe_{1.5}$ | 4.3 | | 19.9 | 19.9 | 22.0 | | 30.7 | 0.0 | 4.6 | -15.9 | | -0.87 | -0.87 |

Notes in Table 2. * For the three runs, 1-3% FeS was added to the starting material; [a] "6+SM1" means 6 wt% of $H_2O$ was added to the starting material SM1, and so forth; [b] Run product mode was obtained from mass balance calculation (data in Tables S1 a-g). Abbreviations: Ol, olivine; Opx, orthopyroxene; Cpx, clinopyroxene; Gt, garnet; Pl, plagioclase; Sp, spinel; [c] Sum of the squares of the residuals was obtained from mass balance calculations with $SiO_2$, $TiO_2$, $Al_2O_3$, MnO, MgO, CaO and $K_2O$ in the run products; [d] Difference between "EPMA difference" $H_2O$ content and the mass balance $H_2O$ content of the quenched glasses; a positive value means water gain and a negative value means water loss during experiment; [e] FeO loss relative, expressed as $100 \cdot (FeO_{calc} - FeO_{starting\ material}) / FeO_{starting\ material}$, in which $FeO_{calc}$ was obtained from mass balance calculation; [f] Oxygen fugacity (expressed as ΔFMQ, Chou, 1987) calculated from the olivine-spinel oxybarometer (Ballhaus et al., 1991); [g] Oxygen fugacity calculated from the AuPdFe alloy and melt compositions (Barr and Grove., 2010). [h] Selected (adopted) $fO_2$ values, see section 4.3 for the details.

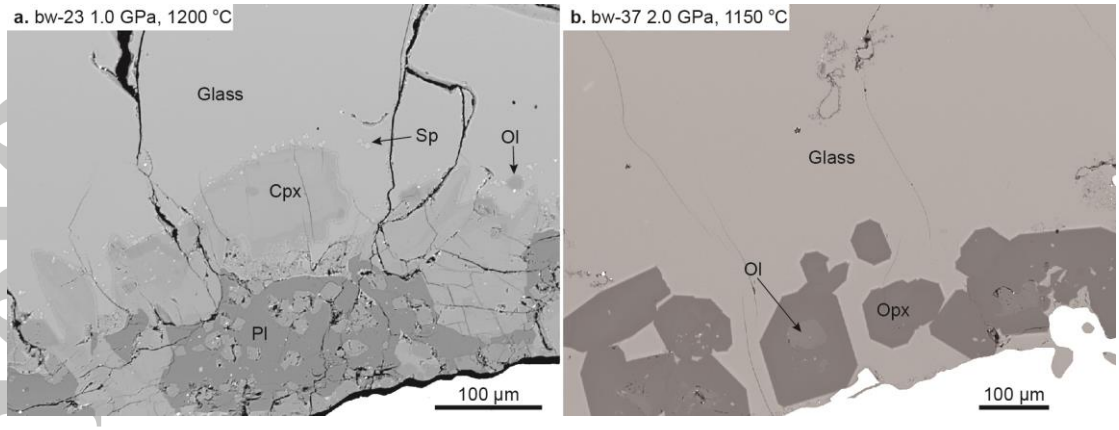


Figure 1. Back-scattered electron (BSE) images of two representative run products, showing large crystals of olivine, opx and cpx, small crystals of spinel and the clear quenched glasses.

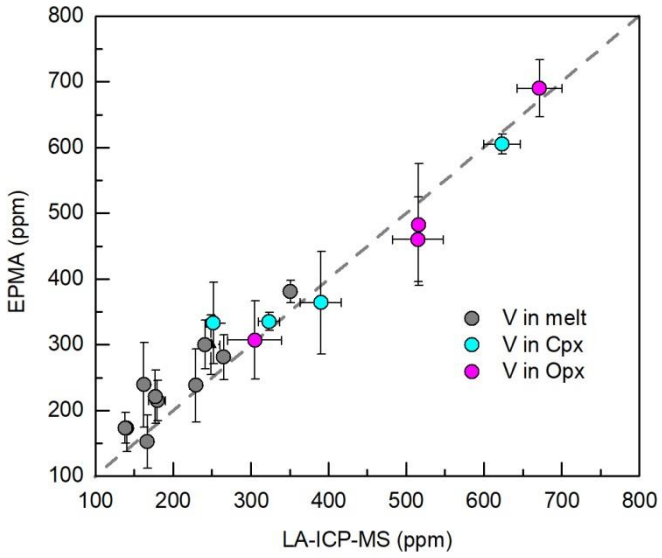


Figure 2. Comparison of V contents in the experimental run products between the LA-ICP-MS and EPMA techniques (data in Table S2 h), indicating good agreement between these two techniques for V contents higher than ~250 ppm.

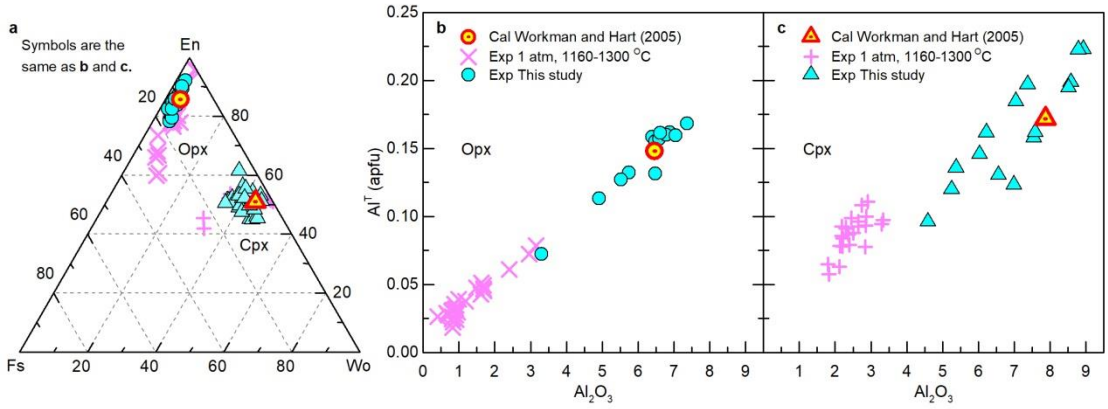


Figure 3. Compositions of opx and cpx synthesized at high pressures (this study, Tables S2 c-d) compared to those synthesized at 1 atm (literature data, Tables S4 e-f) and those in the depleted MORB mantle (DMM, Workman and Hart, 2005). (a): Ternary $CaSiO_3$ (Wo in mole % fraction)-$MgSiO_3$ (En)-$FeSiO_3$ (Fs) diagram, (b) and (c): $Al^T$ (apfu) vs. $Al_2O_3$ (wt%) for opx and cpx. These panels show that pyroxenes synthesized at high pressures and those in the DMM are higher in $Al_2O_3$ and $Al^T$ than those synthesized at 1 atm.

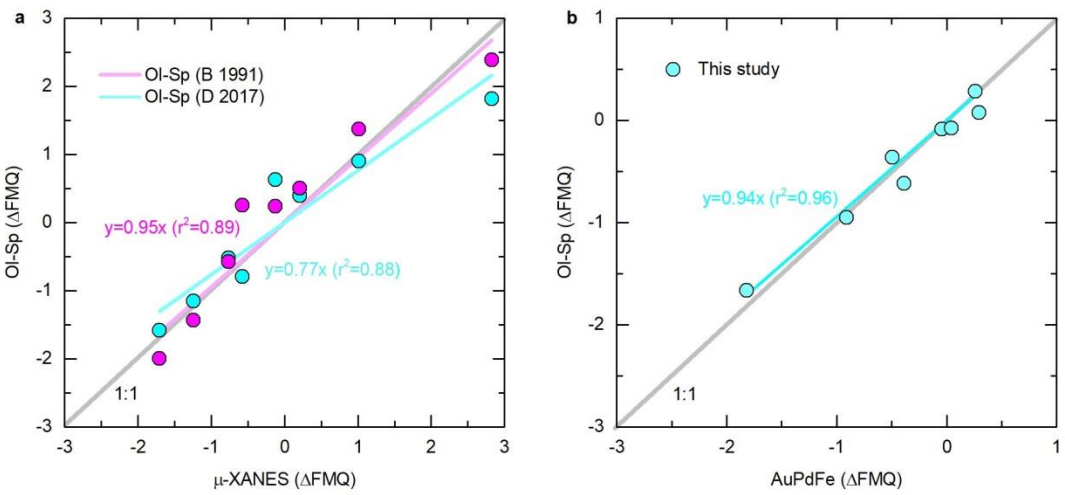


Figure 4. Comparisons of $fO_2$s obtained from different approaches (grey lines represent 1:1 ratio lines). (a) μ-XANES $fO_2$ versus olivine-spinel oxybarometer $fO_2$s (data from 1 atm experiments of Davis and Cottrell, 2018). The magenta and cyan solid circles represent the results of olivine-spinel formulations of Ballhaus et al. (1991) and Davis et al. (2017), respectively. The results indicate accuracy of both of the mineral oxybarometers. (b) A comparison of $fO_2$ values ($fO_2$ < FMQ+0.5, data from this study) obtained from the AuPdFe sensor (Barr and Grove, 2010) with those obtained from the olivine-spinel oxybarometer (Ballhaus et al., 1991). The results indicate high consistency between these two methods (y=0.94x, $r^2$=0.96) when $fO_2$ < FMQ+0.5.

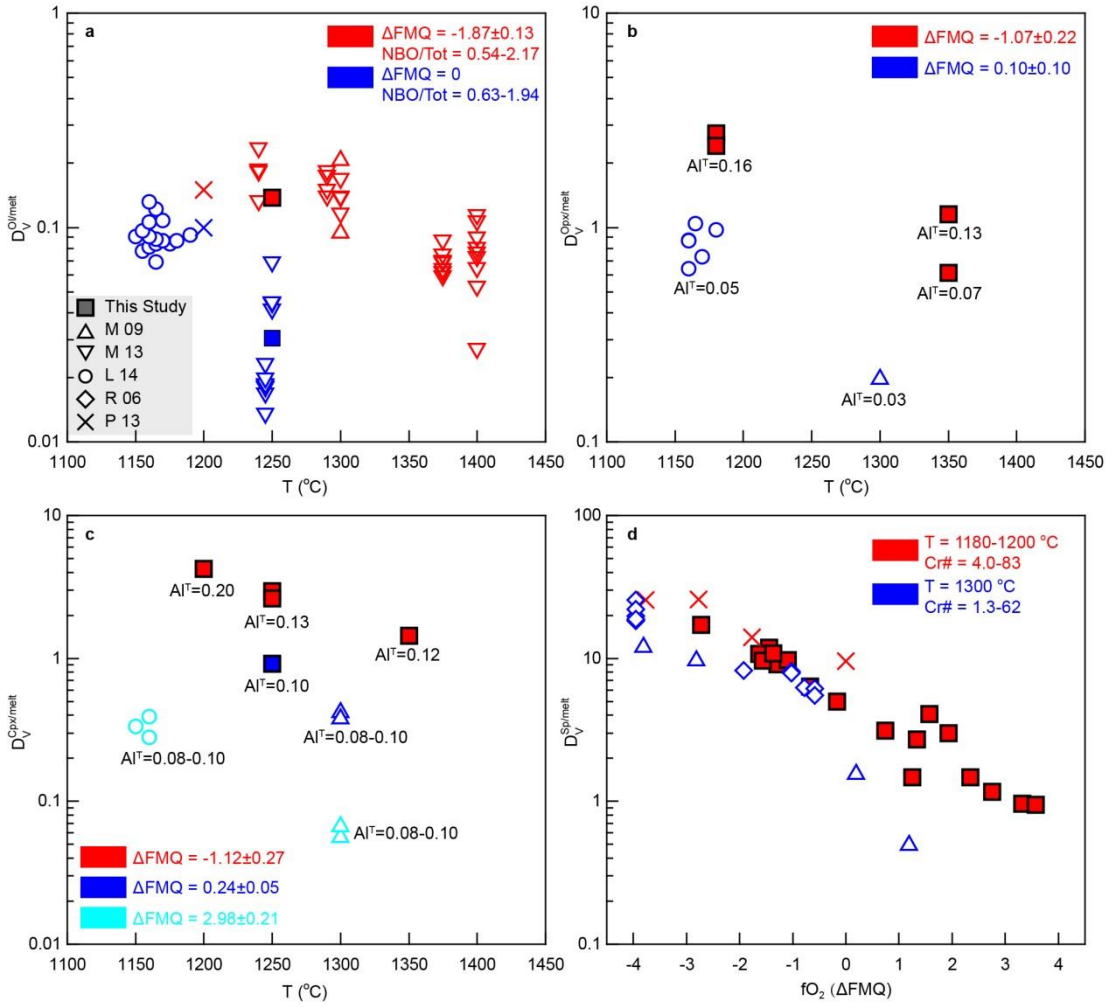


Figure 5. The effect of temperature on $D_V$ values for olivine, opx, cpx and spinel (data from Table S4 a). $D_V$ vs. temperature for olivine (a), opx (b) and cpx (c) is based on the data grouped in terms of small $fO_2$ ranges (variation <±0.25 log units), and $D_V$ vs. $fO_2$ for spinel (d) is based on the two groups of data at 1180-1200°C and 1300°C. These plots show that $D_V$ for each of these four minerals increases with decreasing temperature. The data scatter at a given temperature for each small $fO_2$ range is mainly due to the variation in melt composition (a) or in pyroxene $Al^T$ (b & c), and the data overlap between two temperature groups (d) at a given $fO_2$ is due to the variation of spinel $Cr^{\#}$. Abbreviations: M 09 (Mallmann and O'Neill, 2009); M 13 (Mallmann and O'Neill, 2013); L 14 (Laubier et al., 2014); R 06 (Righter et al., 2006); P 13 (Papike et al., 2013).

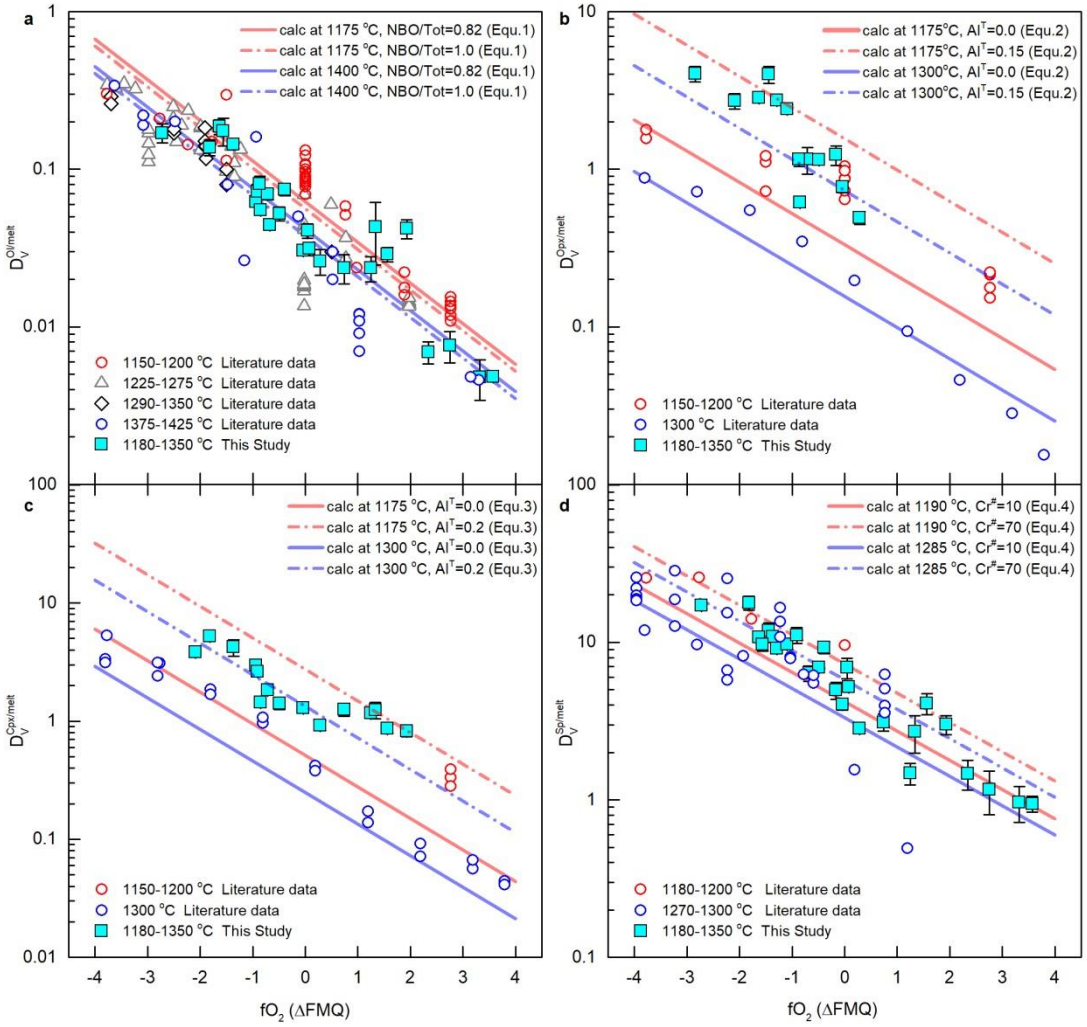


Figure 6. Variations of $D_V$ as a function of $fO_2$ for mantle minerals with data grouped in terms of temperature. The data of all the temperature groups (including ours and published data) are from Tables S4a-g. The red and blue lines represent results calculated at the average temperature and mineral or melt composition of each group using equations 1-4. Both the grouped data (cycles) and the calculated results (lines) show that, in addition to $fO_2$, temperature is another important factor affecting the $D_V$ values for olivine (a), opx (b), cpx (c) and spinel (d). In addition, these panels show that melt composition (NBO/Tot), $Al^T$ in pyroxenes and $Cr^{\#}$ in spinel also has an effect on the $D_V$ for olivine, pyroxenes (opx and cpx) and spinel, respectively.

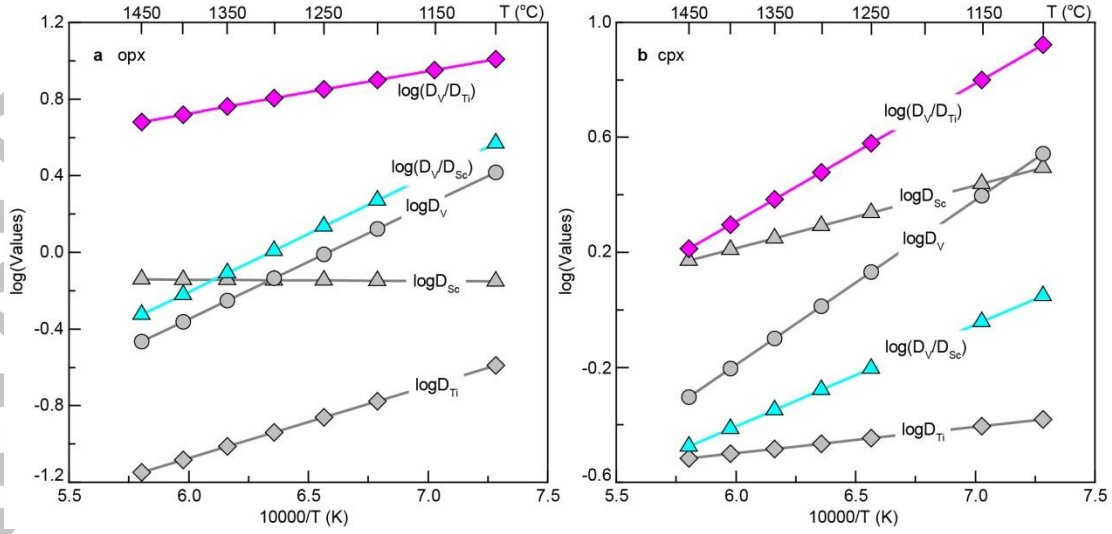


Figure 7. Temperature effect on $D_V$, $D_{Sc}$, $D_{Ti}$, $D_V/D_{Sc}$ and $D_V/D_{Ti}$ for opx (a) and cpx (b). The calculations were performed using equations 2-3 and 5-8 (1 GPa, 1100 to 1450 ℃). In the calculations, $fO_2$ is fixed at FMQ. Mg# of opx is 89.7; $Al^T$ in opx and cpx is 0.15 and 0.17, respectively (Workman 2005). It shows that $D_V$, $D_{Sc}$ and $D_{Ti}$ decrease generally with increasing temperature. What`s more, both $D_V/D_{Sc}$ and $D_V/D_{Ti}$ decrease with increasing temperature, indicating that the temperature-dependence of $D_V$ is greater than that of $D_{Sc}$ and $D_{Ti}$.

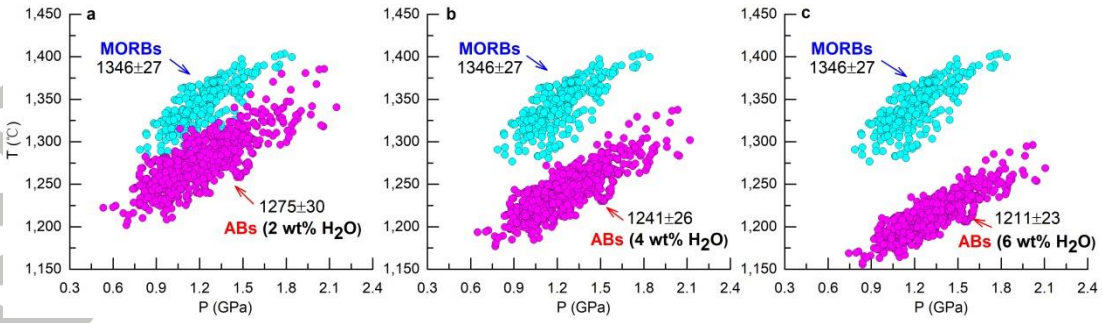


Figure 8. The temperatures and pressures for primitive MORBs and arc basalts (ABs) in equilibrium with $Fo_{90}$ calculated using the melt-thermobarometer (Lee et al., 2009). For MORBs, 0.2 wt% $H_2O$ was used and for arc basalts, $H_2O$ content of 2 wt% (a), 4 wt% (b) and 6 wt% (c) was respectively used in the calculations. The calculated temperatures and pressures of all the collected samples are reported in Tables S5-6. The medians with standard deviations (1σ) of the calculated temperatures of MORBs and ABs are shown in this figure.

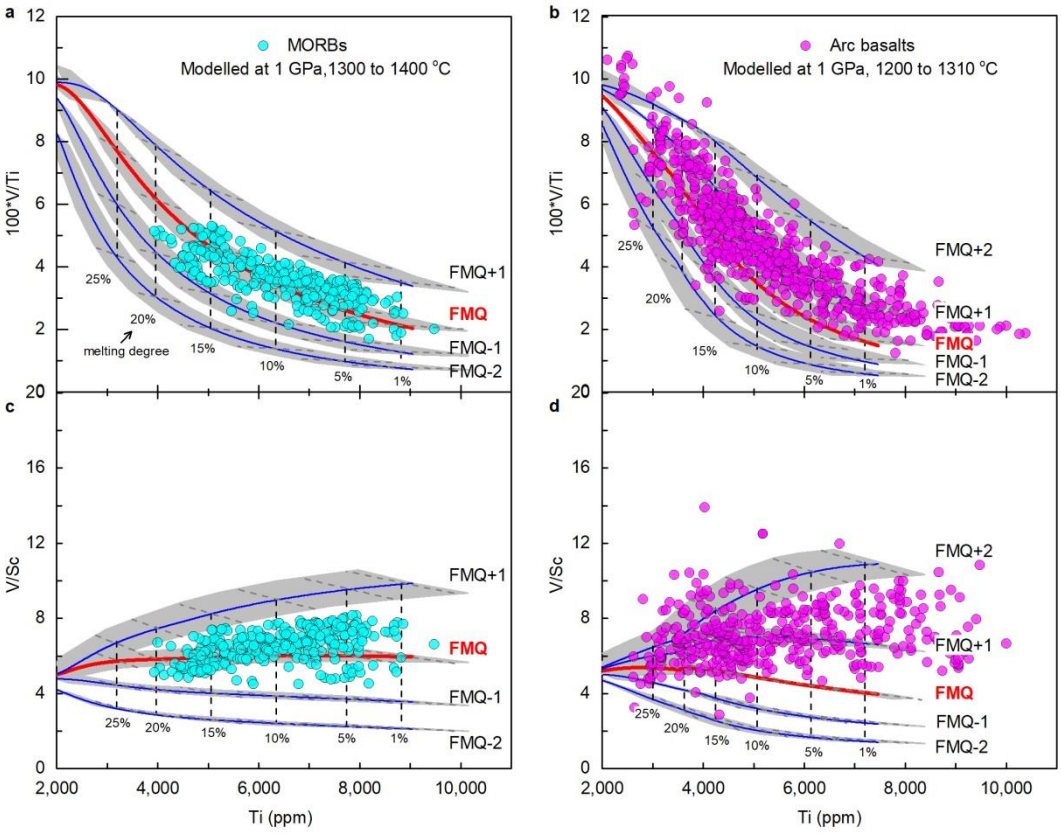


Figure 9. Contrast of the $fO_2$ ranges between primitive arc basalts and MORBs in term of V/Ti and V/Sc ratios and calculated $fO_2$ isopleths during mantle melting at 1.0 GPa. The shaded areas represent the range of elemental ratios when the mantle heterogeneity is considered. Upper and lower bounds of each shaded area are calculated from enriched and depleted mantle sources, respectively. The line in the center of each area is the $fO_2$ isopleth calculated from the normal depleted mantle source. The red lines mark the $fO_2$= FMQ. The vertical dashed lines are melting degree (F) contours calculated from the normal depleted mantle source, whereas the thin oblique dashed lines intersecting with the vertical dashed lines are the F contours calculated from the enriched and depleted mantle sources. This figure shows that (1) V/Sc or V/Ti ratios indeed have significant overlaps between arc basalts (V/Sc = 4.5-10 and 100*V/Ti = 2-11) and MORBs (V/Sc = 4.5-8 and 100*V/Ti = 2-5); (2) even similar V/Sc or V/Ti ratios between arc basalts and MORBs reflect higher arc mantle $fO_2$s due to the lower melting temperatures at arcs relative to at ridges. See text for the calculation details. The modeling routines are reported in Tables S7-8.

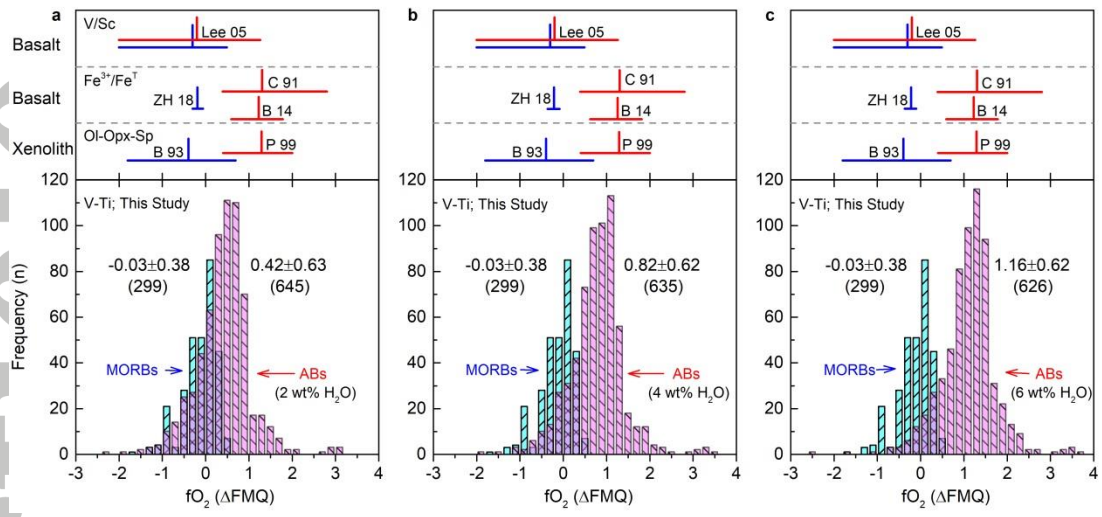


Figure 10. The $fO_2$ ranges and medians of oceanic and arc mantles estimated from V-Ti systematics of primitive basalts. The red areas in a, b, and c represent the calculated $fO_2$s for primitive arc basalts assuming $H_2O$ content of 2, 4 and 6 wt%, respectively. Calculated $fO_2$s for MORBs are shown for comparison in the three panels. Numbers close to the columns are $fO_2$ medians and standard deviation (1σ) of the oceanic and arc samples. The $fO_2$ ranges and medians for oceanic and arc mantles reported by previous studies are shown above this study and V/Sc, $Fe^{3+}/Fe_T$ and Ol-Opx-Sp represent the different $fO_2$ estimation methods used in the previous studies. Abbreviations: B93 (Ballhaus, 1993); B14 (Brounce et al., 2014); C91 (Carmichael, 1991); Lee05 (Lee et al., 2005); P99 (Parkinson and Arculus, 1999); ZH18 (Zhang et al., 2018).

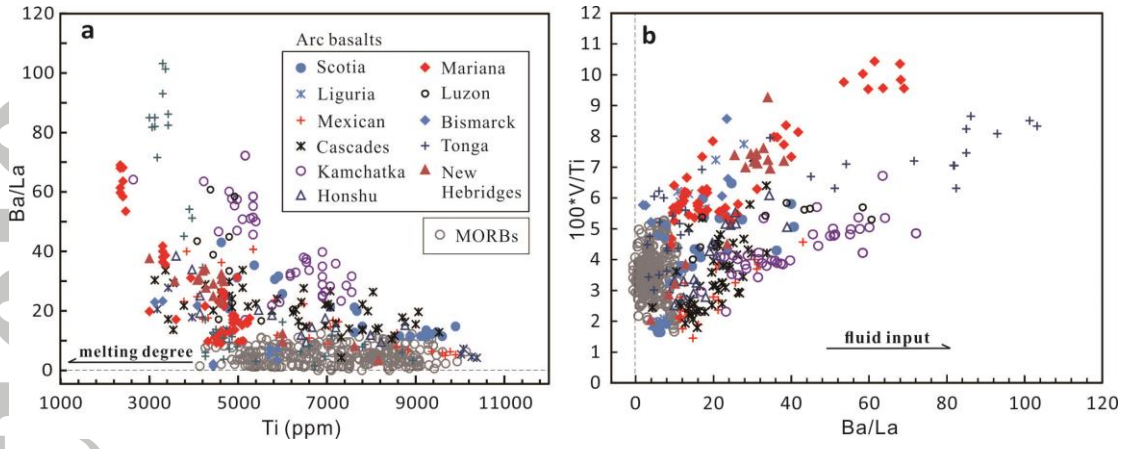


Figure 11. Ba/La vs. Ti (a) and V/Ti vs. Ba/La (b) for primitive MORBs and arc basalts at the 11 arcs. (a) With the increase of mantle melting degree (Ti content in basalt as the proxy of melting degree), Ba/La ratio is invariable in MORBs but increases in the basalts of each arc, indicating Ba/La at arcs reflecting fluid input that depresses the mantle solidus and increases the melting degree. (b) V/Ti (the proxy of $fO_2$) at the basalts of each arc increases with Ba/La, indicating fluid input resulting in oxidization in mantle wedges. Data sources in Tables S5-6.